Research Square

Preprints are preliminary reports that have not undergone peer review.
They should not be considered conclusive, used to inform clinical practice,
or referenced by the media as validated information.

Multi-omics analysis identifies context-dependent roles for integrin α3 in Zika virus oncolytic responses in paediatric neural tumour models

Rob Ewing

rme1a11@soton.ac.uk

University of Southampton https://orcid.org/0000-0001-6510-4001

Yi Sui

University of Southampton

Matthew Sherwood

University of Southampton

Oswaldo Okamoto

Universidade de São Paulo

Yihua Wang

University of Southampton https://orcid.org/0000-0001-5561-0648

Kevin Maringer

Article

Keywords: oncolytic virotherapy, Zika virus (ZIKV), neuroblastoma, pediatric brain tumor, transcriptomics, affinity proteomics, integrin α3

Posted Date: November 13th, 2026

DOI: https://doi.org/10.21203/rs.3.rs-11549766/v1

License: This work is licensed under a Creative Commons Attribution 4.0 International License.
Read Full License

Additional Declarations: Yes there is potential conflict of interest.

Multi-omics analysis identifies context-dependent roles for integrin α3 in Zika virus oncolytic responses in paediatric neural tumour models

Yi Sui[1,2], Matthew Sherwood[1], Oswaldo K. Okamoto[3], Yihua Wang[1], Kevin Maringer[2]*, Rob M. Ewing[1]*

[1] School of Biological Sciences, Faculty of Environmental and Life Sciences, University of Southampton, Southampton, SO17 1BJ, UK

[2] The Pirbright Institute, Ash Road, Pirbright, GU24 0NF, UK

[3] Centro de Estudos do Genoma Humano e Células-Tronco, Departamento de Genética e Biologia Evolutiva, Instituto de Biociências, Universidade de São Paulo, Cidade Universitária, São Paulo, 05508-090, SP, Brazil

* To whom correspondence should be addressed:

Kevin Maringer, kevin.maringer@pirbright.ac.uk

Rob M. Ewing, rob.ewing@soton.ac.uk

Keywords: oncolytic virotherapy, Zika virus (ZIKV), neuroblastoma, pediatric brain tumor, transcriptomics, affinity proteomics, integrin α3

ORCIDs:

Yi Sui: 0009-0007-6214-1844

Matthew Sherwood: 0000-0002-1912-9758

Oswaldo Keith Okamoto: 0000-0002-8528-6225

Yihua Wang: 0000-0001-5561-0648

Kevin Maringer: 0000-0003-0977-8807

Rob M. Ewing: 0000-0001-6510-4001

Abstract

Zika virus (ZIKV), a neurotropic orthoflavivirus, has recently gained attention as a potential oncolytic agent due to its ability to selectively target several neural tumor types and suppress tumor growth in preclinical models. However, the viral and host determinants of this activity remain largely unknown. Here, we used an integrated multi-omics approach, combining RNA-Seq, interaction proteomics and functional assays to uncover mechanisms underlying ZIKV's oncolytic activity in pediatric neural tumors. ZIKV infection reduced the growth and viability of tumorspheres and induced pathways including endoplasmic reticulum stress and immune responses in both neuroblastoma and atypical teratoid rhabdoid tumor (AT/RT) models. Expression of individual ZIKV non-structural (NS) proteins revealed tumour-context-dependent phenotypes: NS4 and NS5 reduced tumorsphere growth in the neuroblastoma and AT/RT models respectively. ZIKV-host protein-protein interaction networks were characterized and we identified that integrin α3 (gene: *ITGA3*), a mediator of cell-matrix adhesion, interacts with ZIKV NS2B and NS4A. Integrin α3 was further shown to modulate ZIKV- and NS4A-induced tumorsphere size reduction, while *ITGA3* knockdown and ZIKV infection additively inhibited 3D invasion. These findings identify context-dependent functional relationships between ZIKV proteins and integrin α3 and define focal-adhesion-associated processes as candidate determinants of ZIKV responses in paediatric neural tumour models.

Introduction

The Zika virus (ZIKV) is an emerging candidate for an oncolytic virotherapy against neural tumours with its neurotropism and ability to cause cell death of tumour cells[1]. ZIKV is an enveloped, positive-sense, single-stranded RNA virus belonging to the genus *Orthoflavivirus* within the family *Flaviviridae*[2]. Its RNA genome encodes three structural proteins, capsid, precursor membrane (prM) and envelope (E), and seven non-structural proteins which collectively regulate entry, replication, particle assembly and interactions with host-cell pathways, including innate immune responses[3–5]. Although infection is asymptomatic in most adults, ZIKV has pronounced neurotropic properties and can cause severe neurological disease, including congenital abnormalities following infection during pregnancy and, more rarely, Guillain–Barré syndrome and other neurological complications[6–8]. These neurotropic properties have prompted considerable interest in exploiting ZIKV against malignancies with neural or neurodevelopmental characteristics.

Studies of ZIKV as an oncolytic agent have consequently focused predominantly on central nervous system (CNS) tumours[1,9,10], particularly glioblastoma, atypical teratoid/rhabdoid tumour (AT/RT) and medulloblastoma[9,11]. AT/RT and medulloblastoma are aggressive paediatric brain tumours, although their susceptibility to ZIKV differs, and we previously demonstrated that ZIKV induces substantially greater cell death in AT/RT cells and tumourspheres than in medulloblastoma models[1]. Neuroblastoma represents another compelling candidate for ZIKV-based oncolytic therapy because of its developmental origin from neural crest-derived cells[12]. Neuroblastoma is a malignancy of the sympathetic nervous system that occurs predominantly in infants and young children, most frequently arising in the adrenal glands or paravertebral sympathetic ganglia[12,13]. It is the most common extracranial solid tumour of childhood and is responsible for approximately 15% of paediatric cancer deaths[14]. Despite growing evidence for the susceptibility of paediatric neural tumours to ZIKV[15,16], the therapeutic potential of ZIKV in neuroblastoma remains comparatively

underexplored. Previous studies have demonstrated ZIKV activity in neuroblastoma using two-dimensional cell cultures and in vivo models[17,18], but its effects in three-dimensional tumour models and, importantly, the molecular mechanisms responsible for these effects remain poorly characterised. Although the consequences of ZIKV infection have been investigated across several tumour types, the contributions of individual ZIKV proteins to anti-tumour phenotypes remain much less well defined. Identifying the viral proteins and host-cell pathways responsible for these effects could uncover determinants of tumour susceptibility and provide a mechanistic basis for developing safer, more selective ZIKV-derived therapeutic strategies.

In this study, we aimed to identify mechanisms underlying ZIKV-mediated oncolysis in paediatric neural tumours by investigating common and distinct responses in neuroblastoma and paediatric brain tumour models. Building on our previous demonstration of ZIKV-mediated oncolysis in 3D AT/RT models[1], we first established its oncolytic activity in 3D neuroblastoma tumourspheres. We then integrated RNA sequencing with analysis of individual ZIKV non-structural proteins and affinity proteomics to identify viral and host factors and protein-protein interactions contributing to the oncolytic phenotype. We identified integrin α3 (*ITGA3*) as an interactor of NS2B and NS4A in both tumour models and found that ITGA3 contributes to ZIKV- and NS4A-mediated reductions in tumoursphere size. Furthermore, *ITGA3* knockdown and ZIKV infection additively suppressed 3D invasion in the AT/RT model but not in neuroblastoma suggesting context- and tumour-specific functions of integrin α3 in ZIKA-mediated oncolysis. Together, these findings identify an ZIKV NS–integrin α3 axis contributing to ZIKV-mediated anti-tumour activity and suggest that targeting integrin-associated pathways could enhance ZIKV-based therapeutic strategies for paediatric neural tumours.

Results

ZIKV exhibits oncolytic effects in neuroblastoma models

To investigate the common mechanisms underlying ZIKV's oncolytic effects in both neuroblastoma and pediatric brain tumors, we first examined its oncolytic effects in neuroblastoma. SH-SY5Y cells, derived from a metastatic bone tumor in a four-year-old patient with non-MYCN-amplified neuroblastoma, and IMR-32 cells, established from an abdominal mass in a 13-month-old patient with MYCN-amplified neuroblastoma[19,20], were infected with either the ZIKV PRVABC59 or BeH819015 strains[21,22] at a multiplicity of infection (MOI) of 2 in monolayer cultures. Cell viability decreased over time in both cell lines following infection with either strain (**Figure S1A and B**). Interestingly, both strains induced earlier virus-mediated cell death in SH-SY5Y cells compared with IMR-32 cells. Virus growth kinetics also revealed a delay in replication in IMR-32 cells compared with SH-SY5Y cells (**Figure S1C and D**).

SH-SY5Y and IMR-32 tumorspheres were subsequently infected with either PRVABC59 or BeH819015 strain at an MOI of 2 or 10. Tumorsphere size was significantly reduced at 8 days post-infection (dpi) following infection with the PRVABC59 strain at both MOIs in both SH-SY5Y (**Figure 1A and B**) and IMR-32 (**Figure 1C and D**) tumorspheres. In contrast, BeH819015 only caused a significant reduction in SH-SY5Y tumorspheres at an MOI of 10. These findings confirm the strong oncolytic effect of the PRVABC59 strain in these experimental systems, which was therefore selected for further investigation. The viability of SH-SY5Y and IMR-32 tumorspheres infected with the PRVABC59 strain at an MOI of 2 or 10 is shown in **Figure 1E and F**. At an MOI of 10, viability dropped to nearly zero by 4 dpi in almost all tumorsphere replicates. However, not all replicates infected at an MOI of 2 exhibited reduced viability even at 6 dpi. To compare viability differences between MOIs, tumorspheres with less or more than 1% viability were counted and replotted (**Figure S1E and F**). This analysis confirmed that a greater proportion of tumorspheres infected at an MOI of 10 had a viability below 1% compared with those infected at an MOI of 2. Virus replication kinetics differed between the two MOIs as well. Virus titers in supernatants from

tumorspheres infected at an MOI of 2 or 10 are shown in **Figure 1G and H**. The proportion of tumorspheres with no detectable virus were calculated and replotted (**Figure S1G and H**), showing that all tumorspheres became infected at an MOI of 10 even from the earliest time points tested, whereas at an MOI of 2 a proportion of tumorspheres failed to get infected even at later time points. These results indicate a binary outcome of infection at an MOI of 2: either the virus established a productive infection and reduced cell viability, or it failed to replicate and viability remained high. In contrast, infection at an MOI of 10 established robust infection in all samples, leading to a consistent drop in cell viability across all tumorspheres.

Transcriptome responses induced by ZIKV infection

To elucidate the mechanisms underlying the ZIKV-induced oncolytic effect, RNA-Seq was performed on SH-SY5Y and IMR-32 neuroblastoma tumorspheres with or without ZIKV infection at an MOI of 10, as this MOI consistently produced a strong and reproducible oncolytic effect. Among the top 30 significantly differentially expressed genes (DEGs), only three were downregulated in SH-SY5Y tumorspheres, while the remainder were upregulated (**Figure 2A, Table S1**). In ZIKV-infected IMR-32 tumorspheres, all 30 of the most significantly altered genes were upregulated (**Figure 2B, Table S2**). These top 30 regulated genes are predominantly associated with endoplasmic reticulum (ER) stress, the unfolded protein response (UPR), oxidative stress, amino acid transport, and immune responses in both cell models. The expression profiles of these genes are consistent with known cellular responses to ZIKV infection and replication[23–26].

To explore common pathways regulated by ZIKV infection in both neuroblastoma and pediatric brain tumor cells, a KEGG pathway analysis was performed (**Figure 2C**). Since ZIKV induces more pronounced cell death in USP7-AT/RT cells compared with other tested pediatric brain tumor cell lines[1], our previously published RNA-Seq data from ZIKV-infected USP7 cells[10] were also reanalyzed and presented within the heatmap. The most significant common pathway across all three cell lines is “Protein processing in endoplasmic reticulum”,

which aligns with the utilisation of the ER for ZIKV replication, protein folding, and assembly[27]. Among the two neuroblastoma cell lines, the altered pathways in SH-SY5Y cells were more similar to the pathways altered in pediatric brain tumor USP7 cells. The common significantly regulated pathways include “TNF signaling pathway”, “Apoptosis”, “Transcriptional misregulation in cancer”, “Lipid and atherosclerosis”, “NF-kappa B signaling pathway”, “Fluid shear stress and atherosclerosis”, and “Protein processing in endoplasmic reticulum”. Overall, these data identify cell line-specific transcriptional changes following ZIKV infection that do not necessarily correlate with the tumor origin of the cell line.

ZIKV NS4A and NS5 suppress tumorsphere formation

Neuroblastoma SH-SY5Y and pediatric brain tumor USP7 cells were then transduced with each of the ZIKV non-structural proteins to investigate each protein’s role in mediating ZIKV’s oncolytic effects. SH-SY5Y cells were selected as they were more permissive to ZIKV infection compared to IMR-32 cells (**Figure 1**). Stable cell lines of SH-SY5Y or USP7 cells expressing GFP (control), NS1-GFP, NS2B-GFP, NS3-GFP, NS4A-GFP, NS4B-GFP, or NS5-GFP were established using lentivirus transduction. Immunofluorescence images (**Figure S2**) and western blot analysis (**Figure S3A and B**) confirmed successful transduction and target protein expression and demonstrated the subcellular localization of each of the non-structural proteins.

Tumorspheres from all established cell lines were then generated and cultured for 12 days. On day 12, GFP alone did not significantly affect the size or viability of SH-SY5Y or USP7 tumorspheres (**Figure 3**). Interestingly, NS1-GFP, NS3-GFP, NS4A-GFP, and NS4B-GFP significantly increased SH-SY5Y tumorsphere area and viability (**Figure 3A-C**), indicating that these non-structural proteins promote tumorsphere formation in neuroblastoma SH-SY5Y cells. In contrast, NS5-GFP significantly reduced both SH-SY5Y tumorsphere area and viability, suggesting an inhibitory effect of ZIKV NS5 on tumorsphere formation. In USP7 tumorspheres, only ZIKV NS4A-GFP significantly reduced both tumorsphere area and viability, while other non-structural proteins had no significant effect (**Figure 3D-F**). These

findings suggest that ZIKV non-structural proteins exert distinct functions across different tumor cell types. NS5 and NS4A are the only non-structural proteins that suppressed tumorsphere formation in neuroblastoma SH-SY5Y and pediatric brain tumor USP7 cells under these experimental conditions, respectively, indicating potential roles for these proteins in ZIKV's oncolytic effects.

Integrated transcriptomics and affinity proteomics analysis identifies integrin α3 as a key factor modulated by ZIKV

To further investigate the mechanisms by which ZIKV non-structural proteins regulate tumorsphere size and contribute to ZIKV's oncolytic effects, affinity proteomics was performed to construct the ZIKV-host protein-protein interaction (PPI) networks for these tumor cells (**Figure 4A**). Mass spectrometry data confirmed that non-structural protein spectral counts were detected in all sample replicates (**Figure S3C**). A total of 345 protein targets and 516 interactions were identified in SH-SY5Y cells (**Figure 4B**; **Table S3**), while 269 protein targets and 344 interactions were identified in USP7 cells (**Figure 4C**; **Table S4**). In total, 79 common interaction partners were shared between the two cell lines (**Figure 5A**), suggesting mostly distinct ZIKV-host interaction profiles across tumor types. NS2B was found to interact with the most common proteins shared between the two cell lines (**Table S5**). To identify key interaction partners common to both tumor types that may contribute to ZIKV's oncolytic effects, comparative analysis of RNA-Seq and NS2B affinity proteomics datasets was performed for NS2B. Overlapping Gene Ontology (GO) cellular component terms between the two datasets revealed that most overlapping terms had previously already been implicated in ZIKV replication, such as "Extracellular exosome"[28], "Cytoplasm"[29], "Endoplasmic reticulum"[27], and "Golgi apparatus"[30] (**Figure 5B**). Interestingly, "Focal adhesion", which plays an important role in connecting tumor cells to the extracellular matrix and facilitating tumor invasion[31], was enriched in both datasets. To further identify the key interaction partners within the "Focal adhesion" cellular component, NS2B's interaction partners enriched in this term were plotted (**Figure 5C**). Among these partners, integrin α3

stood out because it interacts with NS2B in both tumor types and has previously been implicated in regulating cancer progression and metastasis[31–33]. In addition to integrin α3, integrin-linked kinase (gene name: *ILK*), which acts as a scaffold protein at focal adhesions to help link integrins to the actin cytoskeleton[34], also interacts with NS2B in both tumor types. The co-detection of integrin α3 and integrin-linked kinase in the affinity proteomics data strengthens the evidence for an interaction between integrin α3 and NS2B, highlighting integrin α3's potential role in the regulation of ZIKV's oncolytic effects.

Integrin α3 interacts with NS2B and NS4A in both neuroblastoma SH-SY5Y and pediatric brain tumor USP7 cells

To investigate the potential roles of integrin α3 in regulating the changes in tumorsphere size induced by ZIKV non-structural proteins and ZIKV's oncolytic effects, interactions between integrin α3 and ZIKV non-structural proteins were first validated by co-immunoprecipitation (Co-IP). All USP7 cell samples transduced with individual ZIKV non-structural proteins were subjected to immunoprecipitation using GFP-Trap beads, followed by western blotting. The results confirmed an interaction between integrin α3 and NS2B, and NS4A was also found to interact with integrin α3 in USP7 cells (**Figure S4**). Further validation showed that both NS2B and NS4A interacted with integrin α3 and integrin β1, which forms a heterodimer with integrin α3 to constitute the integrin α3β1 complex, in SH-SY5Y and USP7 cells (**Figure 6A-B**).

To determine whether ZIKV non-structural proteins affect the expression levels of these integrins, western blotting was performed. In SH-SY5Y cells, only NS5 significantly reduced the expression of integrin α3 and integrin β1 (**Figure 6C-E**). This finding is consistent with previous research showing that ZIKV NS5 inhibits the migration and invasion of U87 glioma cells[35]. To further explore the role of NS5 in tumor metastasis, the expression level of the epithelial–mesenchymal transition marker vimentin, which has been shown to contribute to tumor invasion and metastasis[36–38], was assessed. Consistent with previous results, NS5

significantly reduced vimentin expression in SH-SY5Y cells (**Figure 6C and F**). However, in USP7 cells, none of the non-structural proteins significantly affected the expression of integrin α3, integrin β1, or vimentin (**Figure 6G-J**). These results suggest that NS5 downregulates integrin α3, integrin β1, and vimentin specifically in SH-SY5Y cells, indicating a potential role for NS5 in inhibiting neuroblastoma invasion. In contrast, NS2B and NS4A do not affect the expression levels of integrin α3 or integrin β1 in either neuroblastoma or pediatric brain tumor cells, despite their physical interactions with these proteins.

To further investigate how integrin α3 influences the protein levels of its interacting partners NS2B and NS4A, *ITGA3* was silenced using siRNA, followed by western blot analysis. siRNA transfection consistently and effectively reduced integrin α3 protein expression in all GFP-expressing, NS2B-expressing, and NS4A-expressing SH-SY5Y and USP7 cells (**Figure S5A-D**). The expression levels of GFP and NS4A remained unchanged in both RISC-Free control and *ITGA3*-knockdown SH-SY5Y and USP7 cells (**Figure 6K-N**). However, NS2B protein levels were significantly increased in *ITGA3*-knockdown cells in both cell lines. No change in NS2B expression was observed in RISC-Free control cells, indicating that the observed effect is not due to off-target effects of the siRNA. These findings suggest that integrin α3 is involved in suppressing NS2B protein levels in both neuroblastoma SH-SY5Y and pediatric brain tumor USP7 cells.

Knockdown of *ITGA3* rescues NS4A-induced reduction in USP7 tumorsphere size

To explore whether integrin α3 is involved in tumorsphere formation regulated by its interaction partners NS2B and NS4A, *ITGA3* was knocked down in wild-type, GFP-expressing, NS2B-expressing, and NS4A-expressing SH-SY5Y and USP7 cells, followed by tumorsphere formation assays. **Figure S5E-H** shows a consistent and effective reduction of integrin α3 protein expression levels in wild-type SH-SY5Y and USP7 cells. In SH-SY5Y cells, *ITGA3* knockdown significantly reduced tumorsphere size in both wild-type and GFP-expressing cells (**Figure 7A**). *ITGA3* knockdown also significantly reduced tumorsphere size of NS2B- and NS4A-expressing SH-SY5Y cells (**Figure 7B**). However, it is unclear whether

these effects are related to interactions between integrin α3 and the non-structural proteins, as *ITGA3* knockdown also reduced tumorsphere size in control cells. In USP7 cells, *ITGA3* knockdown did not affect the tumorsphere size of either wild-type or GFP-expressing cells (**Figure 7C**). There was also no change in the tumorsphere size of NS2B-expressing USP7 cells following *ITGA3* knockdown (**Figure 7D**). However, *ITGA3* knockdown significantly increased the tumorsphere size of NS4A-expressing USP7 cells to the same level observed in untreated wild-type cells. Representative images of tumorspheres from control and NS4A-expressing USP7 cells under different treatments are shown in **Figure 7E and F**. The RISC-Free control had no such effects, indicating that the rescue of NS4A-induced tumorsphere size reduction is specifically due to *ITGA3* knockdown.

Integrin α3 plays different roles in ZIKV's effects on SH-SY5Y and USP7 tumorsphere size

Given integrin α3's interactions with NS2B and NS4A and its role in NS4A-mediated reduction of tumorsphere formation, we hypothesised that integrin α3 may be involved in ZIKV's oncolytic effects. To determine whether ZIKV infection alters integrin α3 protein levels, we assessed its expression and found that ZIKV infection did not significantly change integrin α3 protein levels in either SH-SY5Y or USP7 cells (**Figure S6A-D**).

ITGA3 was then knocked down (**Figure S6E-H**) followed by ZIKV infection to examine changes in cell viability, virus titer and tumorsphere size. *ITGA3* knockdown significantly reduced uninfected cell viability and virus titer in 2D-cultured SH-SY5Y cells (**Figure 8A and B**), but had no effect on viability in the context of ZIKV infection. In line with this finding, in SH-SY5Y tumorspheres *ITGA3* knockdown (confirmed in **Figure S6I-L**) significantly reduced tumorsphere size in non-infected tumorspheres but not during ZIKV infection (**Figure 8C**). Similar corresponding trends in the effects of *ITGA3* knockdown on viability were also observed in tumorspheres, although these differences were not significant (**Figure 8D**). Virus titers in tumorspheres showed no significant change following *ITGA3* knockdown as well (**Figure 8E**). Overall, these findings suggest that while *ITGA3* knockdown has a similar

(though less pronounced) phenotypic effect to ZIKV infection in SH-SY5Y cell monolayers and tumorspheres, the effects of ZIKV infection and *ITGA3* are not additive, and integrin α3 is not required for the ability of ZIKV to shrink tumorsphere size. Nevertheless, ZIKV infection and *ITGA3* knockdown may reduce cell viability and tumorsphere size through shared pathways that are already maximally disrupted during ZIKV infection.

In USP7 cells, *ITGA3* knockdown did not influence cell viability under either ZIKV-infected or non-infected conditions in 2D culture (**Figure 8F**). Integrin α3 also had no notable effects on virus titer, although a marginal statistically significant increase was observed at 2 dpi (**Figure 8G**). Interestingly, in ZIKV-infected USP7 tumorspheres, *ITGA3* knockdown, which had no effect on uninfected tumorspheres, reduced the capacity of ZIKV infection to shrink tumorsphere size (**Figure 8H**). Similarly to our observations in 2D culture, *ITGA3* knockdown did not influence 3D viability under either ZIKV-infected or non-infected conditions (**Figure 8I**), and also did not affect ZIKV titers except for a marginal statistically significant increase at 2 dpi (**Figure 8J**). Taken together, these results suggest that, in contrast to neuroblastoma SH-SY5Y cells, integrin α3 contributes to the ZIKV-induced reduction in pediatric brain tumor USP7 tumorsphere size. These effects are not mediated through impacts on cell viability or viral replication.

ITGA3 knockdown and ZIKV infection additively suppress 3D invasion in USP7 tumorspheres

Integrin α3 is involved in the focal adhesion pathway and mediates cell-matrix interactions. Given its important role in invasion and its interactions with ZIKV non-structural proteins, we investigated whether integrin α3 and ZIKV also functionally interact in a tumor invasion assay. Our transcriptomics data showed that the focal adhesion KEGG pathway was significantly regulated in pediatric brain tumor USP7 cells by ZIKV infection (**Figure 2C**), therefore, *ITGA3* knockdown was performed in USP7 tumorspheres. The results showed that ZIKV infection significantly inhibited USP7 tumorspheres invasion (**Figure 8K and L**), consistent with the transcriptomics data. *ITGA3* knockdown also significantly inhibited

tumorsphere invasion, indicating its important role in this process. When *ITGA3* knockdown was combined with ZIKV infection, invasion was further suppressed compared with either treatment alone. Based on the area ratio of invading cells to spheroid (**Figure 8L**), *ITGA3* knockdown and ZIKV act additively to suppress 3D invasion of USP7 tumorspheres. This was also confirmed by the intensity ratio of invading cells to spheroid when the data were reanalyzed using an alternative method (**Figure S6M**). Therefore, ZIKV-induced suppression of invasion in pediatric brain tumor USP7 tumorspheres is unlikely to be mediated by integrin α3 and the two treatments likely function via independent pathways.

Discussion

Although ZIKV exhibits neural tropism and promising oncolytic properties, its translation into clinical applications requires careful optimization[39]. Strategies such as genetic engineering and combination therapy need to be developed to enhance safety, improve tumor selectivity, and maximize therapeutic potency for effective and controlled treatment[39]. Therefore, understanding the mechanisms underlying ZIKV's oncolytic effects is critical. In this study, we demonstrated that ZIKV infection reduces the size of both SH-SY5Y and IMR-32 neuroblastoma tumorspheres. We also performed a multi-omics analysis to uncover interactions between individual ZIKV non-structural proteins and host factors, as well as the mechanisms driving ZIKV's oncolytic activity in neuroblastoma and AT/RT cell lines. We show that integrin α3 interacts with NS2B and NS4A, and that it regulates the ZIKV-induced oncolytic effects in the USP7 AT/RT model. We also identified a synergistic function of *ITGA3* knockdown combined with ZIKV infection in inhibiting USP7 tumor invasion, providing new insights for potential future combination therapies. Interestingly, the functional interaction between integrin α3 and ZIKV differed between neuroblastoma (SH-SY5Y) and AT/RT (USP7) models, with *ITGA3* knockdown phenocopying the effects of ZIKV infection in SH-SY5Y, albeit that integrin α3 does not contribute to ZIKV-induced impacts on SH-SY5Y cell viability and tumorsphere size.

Before exploring the mechanisms behind ZIKV's oncolytic effects, we first examined whether ZIKV exhibits oncolytic activity in neuroblastoma 3D models. The PRVABC59 ZIKV strain was selected because our previous survey of studies of Zika activity in neuroblastoma cell-lines indicated it as the most promising candidate for neuroblastoma oncolytic virotherapy[16]. Our findings demonstrate its potent oncolytic effect in neuroblastoma 3D models generated from both SH-SY5Y and IMR-32 cell lines, especially compared to the BeH819015 strain, which only significantly reduced SH-SY5Y tumorspheres at an MOI of 10. Interestingly, infection with PRVABC59 at an MOI of 2 produced a binary outcome: either the virus established productive infection and reduced cell viability, or it failed to infect and viability remained high. In contrast, infection at an MOI of 10 consistently established robust infection across all samples, with a consistent decrease in cell viability. These findings indicate that, for future *in vivo* applications or neuroblastoma treatments, selecting the most effective strain and dose is critical.

We also investigated whether individual ZIKV non-structural proteins can exert oncolytic effects in isolation and found that NS4A and NS5 inhibit tumorsphere formation of AT/RT and neuroblastoma cell lines, respectively. NS4A has been reported to induce autophagy and apoptosis[40], and to cause microcephaly by interacting with and inhibiting ANKLE2 as shown in HEK293T cells and *Drosophila* larvae[41]. ZIKV NS5 meanwhile has been reported to significantly inhibit proliferation of the human glioma cell line U87 and suppress tumorigenicity of mouse GL261 glioma cells *in vivo*.[35] Our results show the oncolytic effects of NS4A and NS5 in pediatric neural tumors, consistent with these findings. The differences in non-structural protein function across tumor types suggest the importance of studying their effects in specific target tumors.

Furthermore, we show that integrin α3 interacts with NS2B and NS4A in cell lines of both neuroblastoma and AT/RT, and that it contributes to NS4A-induced oncolytic activity in AT/RT. However, it plays distinct roles in ZIKV-induced oncolytic activities in the two tumor types, which is another interesting finding that underscores the importance of studying the

mechanisms in specific target tumors. Integrin α3 has been implicated in several viral infections. For example, it is an essential host factor for hepatitis E virus (HEV) infection[42]. In hepatocarcinoma cells, *ITGA3* knockout reduces HEV permissibility, as integrin α3 is critical for cellular attachment and entry of the non-enveloped HEV form[42]. Another study showed that the integrin α3β1 heterodimer serves as a cellular receptor for Kaposi's sarcoma-associated herpesvirus entry into Chinese hamster ovary cells[43]. Here, we show for the first time that integrin α3 also regulates the oncolytic effects induced by ZIKV and its protein NS4A. Knockdown of *ITGA3* alone did not significantly affect cell viability in either neuroblastoma or AT/RT cells in 2D or 3D culture models. Although some changes in viral titers were observed following *ITGA3* knockdown, these differences were not significant. These findings indicate that integrin α3 does not play a major role in ZIKV infection and that its roles in ZIKV-induced reduction in tumorsphere size is independent of alterations in cell viability or viral replication. In pediatric brain tumor cells, NS4A may act as a key effector of ZIKV's oncolytic activity, with integrin α3 functioning as a downstream effector of NS4A. However, although integrin α3 interacts with NS4A, *ITGA3* knockdown does not affect NS4A protein levels, and altered NS4A expression does not change integrin α3 protein abundance. Moreover, there is currently no evidence in the literature suggesting that integrin α3 plays a role in ANKLE2-related pathways, and our affinity proteomics data showed no interaction between NS4A and ANKLE2 in either USP7 or SH-SY5Y cells. These findings indicate that the interaction between NS4A and integrin α3 is not regulatory at the level of protein expression but may instead influence functional activities or downstream signaling pathways, and NS4A-induced tumorsphere size reduction may not be related to ANKLE2 regulation.

Integrin α3 forms a heterodimer with integrin β1, which interacts with various extracellular matrix proteins[44], suggesting the potential role of integrin α3 in cancer metastasis. Previous studies have shown that integrin α3 facilitates glioma cell migration and invasion[33], and our results show that integrin α3 contributes to 3D invasion in pediatric brain tumor AT/RT. Moreover, ZIKV infection has been reported to reduce metastasis in AT/RT tumor-bearing

mouse models[1], and our findings show that ZIKV infection reduces 3D invasion in AT/RT tumorspheres. These observations support our transcriptomic and affinity proteomic data, which revealed that ZIKV infection significantly regulates the focal adhesion KEGG pathway (**Figure 2C**) and that its non-structural protein NS2B interacts with host factors involved in focal adhesion cellular component term in AT/RT (**Figure 5B and C**). Interestingly, the combination of ZIKV infection with *ITGA3* knockdown additively suppresses 3D invasion in AT/RT tumorspheres. This indicates that ZIKV-induced reduction in invasion is unlikely to be mediated through integrin α3-mediated signaling pathways and suggests a potential route to combination therapy.

Several limitations should be considered when interpreting the findings of this study. Although our results indicate that integrin α3 contributes to ZIKV- and NS4A-induced reductions in tumorsphere size and *ITGA3* knockdown suppresses 3D invasion in AT/RT tumorspheres, the molecular mechanisms underlying these effects remain incompletely understood. Further studies will be required to define the downstream signaling pathways and cellular processes through which integrin α3 mediates these phenotypic changes. In addition, the protein associations identified by affinity purification–mass spectrometry and subsequently validated by co-immunoprecipitation do not distinguish direct protein–protein binding from indirect associations mediated by additional components of a protein complex. Further biochemical and biophysical studies will therefore be required to determine whether NS2B or NS4A binds directly to integrin α3 and to characterize the relevant interaction interfaces. Finally, the present study relied primarily on *in vitro* models, including established cell lines and 3D tumorspheres. Although these systems provide useful platforms for mechanistic investigation, they do not fully recapitulate the complexity of the tumor microenvironment *in vivo*. Future validation in appropriate *in vivo* models, as well as in patient-derived tumor cells, organoid or co-culture systems, and other primary tumor materials, will be important to establish the physiological and translational relevance of these findings.

Taken together, our findings provide new insights for the improvement of ZIKV's oncolytic effects. We demonstrate the oncolytic roles of ZIKV proteins NS4A and NS5 in pediatric neural tumors and highlight the importance of integrin α3 in ZIKV- and NS4A-induced oncolytic activities. These results suggest that it may be possible to genetically engineer these non-structural proteins to enhance ZIKV's antitumor activity and indicate that ZIKV's oncolytic potency may vary depending on the *ITGA3* expression level in patients' tumors. Additionally, our findings indicate a synergistic effect of ZIKV infection and *ITGA3* knockdown in reducing invasion within our AT/RT tumor model, suggesting the potential of combination strategies involving ZIKV infection and integrin-targeting approaches to inhibit tumor metastasis. However, inhibiting integrin α3 may also reduce ZIKV's oncolytic effects, particularly its effect on tumor size reduction. Therefore, combinatorial treatment strategies involving integrin α3 need to be carefully balanced. Key factors including the sequence of administration and the temporal scheduling of treatments should be evaluated. Further work is needed to explore the potential benefits of exploiting the functional interactions between ZIKV infection and integrin α3 for oncotherapeutics.

Materials and methods

Cell culture

Neuroblastoma SH-SY5Y (CRL-2266) and IMR-32 (CCL-127) cells were purchased from the American Type Culture Collection (ATCC, Manassas, USA). USP7 AT/RT cells were provided and established in-house[1] at the University of São Paulo. HEK293T cells were provided by Nullin Divecha (University of Southampton, Southampton, UK), and Vero cells were provided by Trevor Sweeney (The Pirbright Institute, Pirbright, UK). All cell lines were cultured in medium supplemented with 10% FBS (Thermo Fisher, Waltham, USA, cat. no. 10270106) and 1% penicillin/streptomycin (Thermo Fisher, cat. no. 15140122). The media used for these cells were as follows: SH-SY5Y, HEK293T and Vero: Dulbecco's modified Eagle medium (DMEM) (Thermo Fisher, cat. no. 41966029); IMR-32: Roswell Park Memorial

Institute (RPMI) Medium 1640 with GlutaMAX™ (Thermo Fisher, cat. no. 61870010); USP7: high-glucose DMEM with GlutaMAX™ (Thermo Fisher, cat. no. 61965026). All cell lines were cultured at 37 ℃ in a humidified atmosphere containing 5% CO_2 and were confirmed to be mycoplasma free.

siRNA transfection

For each well of a 6-well plate, siRNAs (QIAGEN, Santa Clarita, CA, USA, cat. no. SI00034174) or RISC-Free control siRNAs (Horizon, Cambridge, UK, cat. no. D-001220-01-05) were transfected into 4 × 10^5 SH-SY5Y cells or 3 × 10^5 USP7 cells using Lipofectamine™ RNAiMAX Transfection Reagent (Thermo Fisher, cat. no. 13778075) at a final concentration of 12.5 nM siRNA per well. Untreated control cells were cultured in complete growth medium. All wells were gently mixed by rocking the plate back and forth and incubated at 37 ℃ in a CO_2 incubator for 42 h before harvesting for downstream assays.

Tumorsphere formation assay

Cells were seeded at 1×10^3 cells per well in 200 µL of medium in 96-well clear ultra-low attachment microplates (Thermo Fisher, cat. no. 10023683) to generate one tumorsphere per well. Images of the tumorspheres were taken daily using an Incucyte® S3 Live-Cell Analysis System (Sartorius, Göttingen, Germany) (Figure 1A and C) and a ZOE Fluorescent Cell Imager (Bio Rad, Hercules, California, USA) (Figure 3A and D; Figure 7E and F), and the area of the tumorspheres was measured using Image J software (version 1.54f; National Institutes of Health, USA; http://imagej.org).

Virus techniques

The ZIKV BeH819015 strain from Brazil was rescued from the infectious cDNA (icDNA) clone icBeH819015 [45], which was provided by Trevor Sweeney (The Pirbright Institute). The ZIKV PRVABC59 (KU501215.1) strain from Puerto Rico was a kind gift from Matt Evans (Icahn School of Medicine at Mount Sinai, New York, USA). Both viral stocks were produced by low MOI infection in Vero cells. For plaque assay titration, Vero cells were seeded in a 48-

well plate at 1.5 x 10^5 cells per well and incubated overnight prior to infection. Ten-fold serial dilutions of viral stocks/samples in serum-free medium was added to each well after the medium was removed, and incubated for 1.5 h at 37 ℃ with shaking every 15-20 min. Vero cells were washed with PBS, and an overlay containing 1% agarose (Invitrogen, Thermo Fisher, cat. no. 16520100) mixed with medium supplemented with 2.5% FBS was added. The Vero cells were then incubated at 37 ℃ in a humidified atmosphere supplemented with 5% CO_2 for 3 days before fixation in 10% formalin (Sigma-Aldrich, Merck, St. Louis, USA, cat. no. HT501128). Cells were stained with 0.1% (w/v) crystal violet (Sigma-Aldrich, cat. no. 61135) for counting.

For infection of 2D cell cultures, cell monolayers were seeded in 96-well plates at 1×10^4 cells per well in 200 µL of medium one day prior to infection. Cells were infected with ZIKV at an MOI of 2 in serum-free medium for 1 h at 37 ℃, then the inoculum was removed and replaced with complete culture medium. Supernatant and cell lysates were collected at the time points as indicated in figures. 3D tumorsphere infection was performed one day after tumorspheres formation for SH-SY5Y and IMR-32 cells, and three days post-tumorsphere formation for USP7 cells. All tumorspheres were infected with ZIKV at an MOI of 2 or 10 for 2 h at 37 ℃. The virus inoculum was removed, tumorspheres were washed with PBS, and then 200 µL of complete culture medium was added to each well. Supernatant and tumorspheres were collected at time points as indicated in figures

Lentivirus transduction

ZIKV non-structural protein plasmid DNA with GFP-Spark tag was purchased from Sino Biological company (Paoli, PA, USA; cat. no. LVCV-35 for vector with GFP-Spark tag only; cat. no. VG40544-ACGLN for NS1-GFP; cat. no. VG40612-ACGLN for NS2B-GFP; cat. no. VG40545-ACGLN for NS3-GFP; cat. no. VG40613-ACGLN for NS4A-GFP; cat. no. VG40614-ACGLN for NS4B-GFP; cat. no. VG40584-ACGLN for NS5-GFP). Bacterial transformation was performed using One Shot™ TOP10 Chemically Competent *E. coli* (Invitrogen, Thermo Fisher, cat. no. C404003) according to the manufacturer's instruction.

Plasmid DNA was isolated using QIAGEN plasmid kits. Lentiviral particles were generated in HEK293T cells using a third-generation packaging system. Briefly, HEK293T cells (1×10^6 cells per well) were seeded in 6-well plates with complete culture media. Viral plasmid and packaging plasmids (Gag-Pol and VSV-G plasmids) purchased from Addgene (Watertown, MA, USA) were mixed at a 4:2:1 ratio in serum-free DMEM and transfected into cells using polyethylenimine (PEI; Merck, Burlington, MA, USA, cat. no. 408719). The culture medium was replaced with fresh complete culture media following overnight incubation at 37 ℃ and viral supernatants were collected at 24, 48 and 72 h post-transfection, clarified by centrifugation at 3000 × g for 15 min, filtered through a 0.45 μm syringe filter, aliquoted, and stored at -80 ℃ until use.

Target cells were plated in 1.5 mL of medium in a 6-well plate and incubated at 37 ℃ prior to infection. Lentivirus stock was mixed with 5 μg/mL polybrene (Sigma-Aldrich, cat. no. 107689-10G) for infection and cells were incubated overnight, after which the medium was replaced with complete culture medium. After an additional 48 h, the cells were passaged and collected into a flask. Cells expressing GFP were selected using the Bigfoot cell sorter (Thermo Fisher) and bulked up to generate stable cell lines expressing GFP negative control, NS1-GFP, NS2B-GFP, NS3-GFP, NS4A-GFP, NS4B-GFP, or NS5-GFP.

Viability assay

Viability of 2D cell monolayers and 3D tumorspheres was measured using the CellTiter-Glo® Luminescent Cell Viability Assay kit (Promega, Madison, WI, USA, cat. no. G7570) or the CellTiter-Glo® 3D Cell Viability Assay (Promega, cat. no. G9683), following the manufacturer's instructions. Luminescence was measured using the GloMax®-Multi + Detection System (Promega). Cell (3D) viability was calculated using the following equation:

$$\text{Cell (3D) viability (\%)} = \left(\frac{\text{luminescence of infected sample} - \text{average luminescence of media}}{\text{average luminescence of mock} - \text{average luminescence of media}}\right) \times 100\%$$

All viability data were normalized to the average data at 0 dpi.

3D invasion assay

Tumorspheres were formed and infected as described above prior to the addition of invasion matrix (Bio-Techne, Minneapolis, MN, USA, cat. no. 3500-096-03) on ice. Plates were centrifuged at 300 × g at 4 ℃ for 5 min and incubated at 37 ℃ for 1 h. Plates were incubated at 37 ℃ in a humidified atmosphere with 5% CO_2 for 4 days prior to imaging. Images were captured using the Incucyte® S3 Live-Cell Analysis System (Sartorius). Spheroid area and invading cell area were quantified using the system. Mean intensity of spheroids and invading cells was quantified using image J software (version 1.54f; National Institutes of Health, USA; http://imagej.org).

Confocal microscopy

Wild-type or lentivirus-transduced SH-SY5Y or USP7 cells were seeded on coverslips (0.16-0.19 mm thickness) overnight to allow attachment. Coverslips were then washed with PBS and fixed with 4% PFA (diluted in PBS) at room temperature for 15 min. After washing with PBS, 0.1% Triton X-100 (Sigma Aldrich, cat. no. T8787) (diluted in PBS) was added for permeabilization at room temperature for 15 min. After washing again with PBS, coverslips were stained with DAPI (Invitrogen, Thermo Fisher, cat. no. D1306, 1:2000) at room temperature for 10 min, protected from light, then washed three times with PBS for 10 min in the dark. Rhodamine phalloidin (Invitrogen, Thermo Fisher, cat. no. R415, 1:1000) was added to stain F-actin at room temperature for 1 h, protected from light. Coverslips were then washed three times with PBS for 10 min in the dark, mounted with Fluoromount-G™ mounting medium (Invitrogen, Thermo Fisher, cat. no. 00-4958-02), and stored in the dark at 4 ℃ after dry until imaging. Images were captured using a Leica SP8 confocal microscope (Leica Microsystems, Wetzlar, Germany).

Co-immunoprecipitation

Wild-type or lentivirus-transduced SH-SY5Y or USP7 cells were seeded in 100 mm dishes at a density of 1 x 10^7 cells per dish. Cells were harvested by scraping into ice-cold PBS and centrifuged at 500 × g for 3 min at 4 ℃. The supernatant was discarded, and the cell pellet was washed twice more by gentle resuspension in ice-cold PBS. Cell lysis and immunoprecipitation were conducted using the ChromoTek GFP-Trap® Agarose kit (Proteintech, Manchester, UK, cat. no. gta) according to the manufacturer's instruction.

Western blot

Wild-type or lentivirus-transduced SH-SY5Y or USP7 cells were seeded in 6-well plates at a density of 6 x 10^5 cells per well. All samples were kept on ice throughout the procedure. Cells were washed twice with PBS, and 120 µl of ice-cold RIPA lysis buffer (Thermo Fisher, cat. no. 89900), supplemented with 1× Halt™ Protease Inhibitor Cocktail and 1× EDTA (Thermo Fisher, cat. no. 87786), was added to each well. Plates were kept on ice for 5 min with intermittent pipetting, followed by sonication for 5 min. Lysates were then centrifuged at 14,000 × g for 15 min at 4 ℃, and the supernatant was collected and mixed thoroughly. Protein concentration was determined using the Bradford assay. LDS sample buffer (Thermo Fisher, cat. no. NP0007), supplemented with 5% 2-mercaptoethanol (Sigma Aldrich, cat. no. M6250), was added to lysates and samples were boiled at 100 ℃ for 5 min. Samples were subjected to SDS-PAGE and then transferred on to 0.45 µm nitrocellulose membranes (Thermo Fisher, cat. no. 88018).

Membranes were stained with Ponceau S solution (Sigma Aldrich, cat. no. P7170-1L), washed with Tris-buffered saline with Tween 20 (TBST), and blocked with 5% milk powder (Marvel, Premier Foods, UK) for 1 h. Membranes were then incubated overnight at 4 ℃ with the following primary antibodies: GFP (Cell Signaling Technology, Danvers, MA, USA, cat. no. 2956, 1:1000), integrin α3 (Proteintech, cat. no. 66070-1-Ig, 1:1000), integrin β1 (Proteintech, cat. no. 12594-1-AP, 1:1000), vimentin (Cell Signaling Technology, cat. no. 5741, 1:1000), and GAPDH (Cell Signaling Technology, cat. no. 2118, 1:1000). After three 10-min washes with TBST, membranes were incubated for 1 h at room temperature with one

of the following secondary antibodies: IRDye® 680LT Goat anti-Rabbit IgG (LI-COR Biosciences, Lincoln, NE, USA, cat. no. 926-68021, 1:5000), IRDye® 800CW Goat anti-Rabbit IgG (LI-COR Biosciences, cat. no. 926-32211, 1:5000), IRDye® 680LT Goat anti-Mouse IgG (LI-COR Biosciences, cat. no. 926-68020, 1:5000), and IRDye® 800CW Goat anti-Mouse IgG (LI-COR Biosciences, cat. no. 926-32210, 1:5000). Membranes were washed again three times with TBST and imaged using the LI-COR Odyssey Western Blot imager (LI-COR Biosciences). Quantification was performed using Image J software (version 1.54f; National Institutes of Health, USA; http://imagej.org).

RNA-Seq and data analysis

Tumorsphere samples were collected into TRIzol (Thermo Fisher, cat. no. 15596018), and total RNA was extracted according to the manufacturer's instruction. mRNA sequencing was conducted by Novogene company (Beijing, China). Raw RNA-Seq reads were quality-checked using FastQC (version 0.11.9) and trimmed with Trim Galore (version 0.6.10). Post-trim quality was checked again with FastQC. Trimmed reads were then aligned against the *Homo sapiens* GRCh38 reference genome using HISAT2 (version 2.2.1). Samtools (version 1.16.1) and Subread (featureCounts, version 2.0.6) were used to generate count tables. DESeq2 (version 1.42.1) was used for differential gene expression analysis. Significance was adjusted using the Benjamini-Hochberg method. Official gene symbols of significant DEGs (padj < 0.05) were submitted to the Database for Annotation, Visualisation and Integration Discovery (DAVID) online bioinformatics resources (https://david.ncifcrf.gov/) for KEGG pathway analysis.

Affinity purification-mass spectrometry (AP-MS) and data analysis

SH-SY5Y or USP7 cells expressing GFP alone or GFP-tagged non-structural protein were collected, washed with PBS, and lysed as described in the Co-IP method. Immunoprecipitation, washing, and subsequent on-bead digestion were performed as previously described[46] using GFP-Trap Agarose beads (Chromotex, Proteintech, cat. no.

gtma). Reversed-phase nano-liquid chromatography-tandem mass spectrometry was performed as previously described[46] using a nano-Ultimate 3000 liquid chromatography system coupled to a Lumos Fusion mass spectrometer (both Thermo Fisher).

Raw mass spectrometry data were processed using MSFragger within the FragPipe platform and searched against the UniProtKB human proteome (proteome ID: UP000005640) spiked with GFP and ZIKV non-structural protein sequences. Quantitative outputs from MSFragger were analyzed using the LIMMA package (https://github.com/wasimaftab/LIMMA-pipeline-proteomics)[47] in R. Protein lists after the analysis were then submitted to Significance Analysis of Interactome (SAINT) and Contaminant Repository for Affinity Purification (CRAPome) online analysis (http://www.crapome.org/). Common nonspecific GFP-tag interactors were removed using a CRAPome frequency cutoff > 60%. SAINT probability (SP) score = 1 for SH-SY5Y and SP score ≥ 0.85 for USP7 were set as thresholds for high-confidence interactions. Official gene symbols of high-confidence interacting proteins were then submitted to the DAVID for GO analysis. High-confidence interacting proteins were mapped using Cytoscape software (version 3.9.1).

Statistical analysis

Statistical analyses for plaque assay titration and functional assays were conducted in GraphPad Prism (version 10.3.1; GraphPad Software, San Diego, CA, USA) using one-way ANOVA with Dunnett's T3 multiple comparisons test, two-way ANOVA with Holm-Šidák multiple comparisons test, or Student's *t*-test. padj < 0.05 for RNA-Seq analysis and $p < 0.05$ for all other analyses were considered statistically significant. "padj" represents the adjusted *p*-value calculated using the Benjamini-Hochberg method.

Data availability

RNA-Seq data have been deposited in the NCBI Gene Expression Omnibus (GEO) under accession number GSE313773. The mass spectrometry proteomics data have been

deposited to the ProteomeXchange Consortium via the PRIDE[48] partner repository with the dataset identifier PXD077091.

Acknowledgements

We thank Jinhui Gao for technical support with the experiments. We also thank Dr Alexander von Kriegsheim's research group at the University of Edinburgh for performing the mass spectrometry work. This work was supported by grants from Neuroblastoma UK, The Rosetrees Trust, The Little Princess Trust and MRC MR/S01411X/1. Y.S. was supported by the China Scholarship Council (grant no. 202106350031). Work performed at The Pirbright Institute was supported by BBSRC grants BBS/E/PI/230002B and BBS/E/PI/23NB0003.

Author contributions

Y.S. and R.M.E. conceptualized the approaches used, with input from K.M., O.K.O., and Y.W. Experiments and data analysis were conducted by Y.S., with assistance from M.S., who prepared lentivirus stocks and performed lentivirus transduction in USP7 cells, as well as cell lysis for transduced USP7 cells before AP-MS. Y.S. wrote the original manuscript, and all authors reviewed and edited it.

Declaration of interests

O.K.O is an advisor at Vyro biotherapeutics. All other authors declare no competing interests.

References

1. Kaid, C., Goulart, E., Caires-Júnior, L.C., Araujo, B.H.S., Soares-Schanoski, A., Bueno, H.M.S., Telles-Silva, K.A., Astray, R.M., Assoni, A.F., Júnior, A.F.R., et al. (2018). Zika Virus Selectively Kills Aggressive Human Embryonal CNS Tumor Cells In Vitro and In Vivo. Cancer Res *78*, 3363–3374. https://doi.org/10.1158/0008-5472.CAN-17-3201.

2. Mwaliko, C., Nyaruaba, R., Zhao, L., Atoni, E., Karungu, S., Mwau, M., Lavillette, D., Xia, H., and Yuan, Z. Zika virus pathogenesis and current therapeutic advances. Pathog Glob Health *115*, 21–39. https://doi.org/10.1080/20477724.2020.1845005.

3. Shankar, A., Patil, A.A., and Skariyachan, S. (2017). Recent Perspectives on Genome, Transmission, Clinical Manifestation, Diagnosis, Therapeutic Strategies, Vaccine Developments, and Challenges of Zika Virus Research. Front Microbiol *8*, 1761. https://doi.org/10.3389/fmicb.2017.01761.

4. Roozitalab, A., Zhang, J., Zhang, C., Tang, Q., and Zhao, R.Y. (2025). The Evolving Role of Zika Virus Envelope Protein in Viral Entry and Pathogenesis. Viruses *17*, 817. https://doi.org/10.3390/v17060817.

5. Roy, A., Liu, Q., Yang, Y., Debnath, A.K., and Du, L. (2024). Envelope Protein-Targeting Zika Virus Entry Inhibitors. Int J Mol Sci *25*, 9424. https://doi.org/10.3390/ijms25179424.

6. Maduka-Ezeh, A.N. (2016). Zika Virus – An Obscure Disease Goes "Viral." Dela J Public Health *2*, 6–13. https://doi.org/10.32481/djph.2016.04.003.

7. Krauer, F., Riesen, M., Reveiz, L., Oladapo, O.T., Martínez-Vega, R., Porgo, T.V., Haefliger, A., Broutet, N.J., and Low, N. (2017). Zika Virus Infection as a Cause of Congenital Brain Abnormalities and Guillain–Barré Syndrome: Systematic Review. PLoS Med *14*, e1002203. https://doi.org/10.1371/journal.pmed.1002203.

8. Muñoz, L.S., Parra, B., and Pardo, C.A. (2017). Neurological Implications of Zika Virus Infection in Adults. J Infect Dis *216*, S897–S905. https://doi.org/10.1093/infdis/jix511.

9. Zhu, Z., Gorman, M.J., McKenzie, L.D., Chai, J.N., Hubert, C.G., Prager, B.C., Fernandez, E., Richner, J.M., Zhang, R., Shan, C., et al. (2017). Zika virus has oncolytic activity against glioblastoma stem cells. J Exp Med *214*, 2843–2857. https://doi.org/10.1084/jem.20171093.

10. Sherwood, M., Mitsugi, T.G., Kaid, C., Coke, B., Zatz, M., Maringer, K., Okamoto, O.K., and Ewing, R.M. (2025). Multi-omics analysis reveals key immunogenic signatures induced by oncolytic Zika virus infection of paediatric brain tumour cells. Sci Rep *15*, 13090. https://doi.org/10.1038/s41598-025-97804-8.

11. Chen, Q., Wu, J., Ye, Q., Ma, F., Zhu, Q., Wu, Y., Shan, C., Xie, X., Li, D., Zhan, X., et al. (2018). Treatment of Human Glioblastoma with a Live Attenuated Zika Virus Vaccine Candidate. *9*, 13.

12. Luksch, R., Castellani, M.R., Collini, P., De Bernardi, B., Conte, M., Gambini, C., Gandola, L., Garaventa, A., Biasoni, D., Podda, M., et al. (2016). Neuroblastoma (Peripheral neuroblastic tumours). Critical Reviews in Oncology/Hematology *107*, 163–181. https://doi.org/10.1016/j.critrevonc.2016.10.001.

13. Hoehner, J.C., Gestblom, C., Hedborg, F., Sandstedt, B., Olsen, L., and Påhlman, S. (1996). A developmental model of neuroblastoma: differentiating stroma-poor tumors' progress along an extra-adrenal chromaffin lineage. Lab Invest *75*, 659–675.

14. Park, J.R., Eggert, A., and Caron, H. (2010). Neuroblastoma: Biology, Prognosis, and Treatment. Hematology/Oncology Clinics of North America *24*, 65–86. https://doi.org/10.1016/j.hoc.2009.11.011.

15. Kaid, C., Madi, R.A.D.S., Astray, R., Goulart, E., Caires-Junior, L.C., Mitsugi, T.G., Moreno, A.C.R., Castro-Amarante, M.F., Pereira, L.R., Porchia, B.F.M.M., et al. (2020). Safety, Tumor Reduction, and Clinical Impact of Zika Virus Injection in Dogs with Advanced-Stage Brain Tumors. Mol Ther *28*, 1276–1286. https://doi.org/10.1016/j.ymthe.2020.03.004.

16. Sherwood, M., Zhou, Y., Sui, Y., Wang, Y., Skipp, P., Kaid, C., Gray, J., Okamoto, K., and Ewing, R.M. (2023). Integrated re-analysis of transcriptomic and proteomic datasets reveals potential mechanisms for Zika viral-based oncolytic therapy in neuroblastoma. Preprint at F1000Research, https://doi.org/10.12688/f1000research.132627.2 https://doi.org/10.12688/f1000research.132627.2.

17. Mazar, J., Li, Y., Rosado, A., Phelan, P., Kedarinath, K., Parks, G.D., Alexander, K.A., and Westmoreland, T.J. (2018). Zika virus as an oncolytic treatment of human neuroblastoma cells requires CD24. PLoS One *13*, e0200358. https://doi.org/10.1371/journal.pone.0200358.

18. Mazar, J., Brooks, J.K., Peloquin, M., Rosario, R., Sutton, E., Longo, M., Drehner, D., and Westmoreland, T.J. (2024). The Oncolytic Activity of Zika Viral Therapy in Human Neuroblastoma In Vivo Models Confers a Major Survival Advantage in a CD24-dependent Manner. Cancer Res Commun *4*, 65–80. https://doi.org/10.1158/2767-9764.CRC-23-0221.

19. Tumilowicz, J.J., Nichols, W.W., Cholon, J.J., and Greene, A.E. (1970). Definition of a continuous human cell line derived from neuroblastoma. Cancer Res *30*, 2110–2118.

20. Ross, R.A., Spengler, B.A., and Biedler, J.L. (1983). Coordinate morphological and biochemical interconversion of human neuroblastoma cells. J Natl Cancer Inst *71*, 741–747.

21. Mutso, M., Saul, S., Rausalu, K., Susova, O., Žusinaite, E., Mahalingam, S., and Merits, A. (2017). Reverse genetic system, genetically stable reporter viruses and packaged subgenomic replicon based on a Brazilian Zika virus isolate. J Gen Virol *98*, 2712–2724. https://doi.org/10.1099/jgv.0.000938.

22. Widman, D.G., Young, E., Yount, B.L., Plante, K.S., Gallichotte, E.N., Carbaugh, D.L., Peck, K.M., Plante, J., Swanstrom, J., Heise, M.T., et al. (2017). A Reverse Genetics Platform That Spans the Zika Virus Family Tree. mBio *8*, e02014-16. https://doi.org/10.1128/mBio.02014-16.

23. Mohd Ropidi, M.I., Khazali, A.S., Nor Rashid, N., and Yusof, R. (2020). Endoplasmic reticulum: a focal point of Zika virus infection. J Biomed Sci *27*, 27. https://doi.org/10.1186/s12929-020-0618-6.

24. Lebeau, G., Turpin, J., Frumence, E., El Safadi, D., Harrabi, W., Desprès, P., Krejbich-Trotot, P., and Viranaïcken, W. (2022). Evidence of RedOX Imbalance during Zika Virus Infection Promoting the Formation of Disulfide-Bond-Dependent Oligomers of the Envelope Protein. Viruses *14*, 1131. https://doi.org/10.3390/v14061131.

25. Almeida, L.T., Ferraz, A.C., da Silva Caetano, C.C., da Silva Menegatto, M.B., dos Santos Pereira Andrade, A.C., Lima, R.L.S., Camini, F.C., Pereira, S.H., da Silva Pereira, K.Y., de Mello Silva, B., et al. (2020). Zika virus induces oxidative stress and decreases antioxidant enzyme activities *in vitro* and *in vivo*. Virus Research *286*, 198084. https://doi.org/10.1016/j.virusres.2020.198084.

26. Lee, L.J., Komarasamy, T.V., Adnan, N.A.A., James, W., and RMT Balasubramaniam, V. (2021). Hide and Seek: The Interplay Between Zika Virus and the Host Immune Response. Front Immunol *12*, 750365. https://doi.org/10.3389/fimmu.2021.750365.

27. Rothan, H.A., and Kumar, M. (2019). Role of Endoplasmic Reticulum-Associated Proteins in Flavivirus Replication and Assembly Complexes. Pathogens *8*, 148. https://doi.org/10.3390/pathogens8030148.

28. Velázquez-Cervantes, M.A., Flores-Pliego, A., Benitez-Zeferino, Y.R., Cruz-Holguín, V.J., Herrera Moro-Huitron, L., Helguera-Repetto, A.C., Meza-Sánchez, D.E., Maravillas-Montero, J.L., Cayetano-Castro, N., Mancilla-Ramírez, J., et al. (2025). Zika Virus Infection Modulates Extracellular Vesicle Biogenesis and Morphology in Human Umbilical Cord Endothelial Cells: A Proteomic and Microscopic Analysis. Microorganisms *13*, 1402. https://doi.org/10.3390/microorganisms13061402.

29. Denolly, S., Stukalov, A., Barayeu, U., Rosinski, A.N., Kritsiligkou, P., Joecks, S., Dick, T.P., Pichlmair, A., and Bartenschlager, R. (2023). Zika virus remodelled ER membranes contain proviral factors involved in redox and methylation pathways. Nat Commun *14*, 8045. https://doi.org/10.1038/s41467-023-43665-6.

30. Kumar, P., Kumar, L.K., and Singh, P.K. (2025). Zika virus triggers Golgiphagy and remodels the Golgi apparatus to facilitate viral replication in human trabecular meshwork cells. Invest. Ophthalmol. Vis. Sci. *66*, 3524–3524.

31. Zhu, W., Pan, S., Xu, J., Wang, Y., Fu, Z., Han, X., Zhang, Y., Zhao, Q., Zhang, R., Hu, C., et al. (2025). Inhibition of integrin α3 suppresses gastric cancer progression via STAT3-mediated regulation of SLC1A5-dependent glutamine uptake. J Gastroenterol. https://doi.org/10.1007/s00535-025-02305-0.

32. Du, Q., Wang, W., Liu, T., Shang, C., Huang, J., Liao, Y., Qin, S., Chen, Y., Liu, P., Liu, J., et al. (2020). High Expression of Integrin α3 Predicts Poor Prognosis and Promotes Tumor Metastasis and Angiogenesis by Activating the c-Src/Extracellular Signal-Regulated Protein Kinase/Focal Adhesion Kinase Signaling Pathway in Cervical Cancer. Front. Oncol. *10*. https://doi.org/10.3389/fonc.2020.00036.

33. Nakada, M., Nambu, E., Furuyama, N., Yoshida, Y., Takino, T., Hayashi, Y., Sato, H., Sai, Y., Tsuji, T., Miyamoto, K. -i, et al. (2013). Integrin α3 is overexpressed in glioma stem-like cells and promotes invasion. Br J Cancer *108*, 2516–2524. https://doi.org/10.1038/bjc.2013.218.

34. Qin, J., and Wu, C. (2012). ILK: a pseudokinase in the center stage of cell-matrix adhesion and signaling. Curr Opin Cell Biol *24*, 607–613. https://doi.org/10.1016/j.ceb.2012.06.003.

35. Li, H., Hu, Y., Huang, J., Feng, Y., Zhang, Z., Zhong, K., Chen, Y., Wang, Z., Huang, C., Yang, H., et al. (2019). Zika virus NS5 protein inhibits cell growth and invasion of glioma. Biochem Biophys Res Commun *516*, 515–520. https://doi.org/10.1016/j.bbrc.2019.06.064.

36. Grasset, E.M., Dunworth, M., Sharma, G., Loth, M., Tandurella, J., Cimino-Mathews, A., Gentz, M., Bracht, S., Haynes, M., Fertig, E.J., et al. (2022). Triple negative breast cancer metastasis involves complex EMT dynamics and requires vimentin. Sci Transl Med *14*, eabn7571. https://doi.org/10.1126/scitranslmed.abn7571.

37. Wei, J., Xu, G., Wu, M., Zhang, Y., Li, Q., Liu, P., Zhu, T., Song, A., Zhao, L., Han, Z., et al. (2008). Overexpression of vimentin contributes to prostate cancer invasion and metastasis via src regulation. Anticancer Res *28*, 327–334.

38. Berr, A.L., Wiese, K., dos Santos, G., Koch, C.M., Anekalla, K.R., Kidd, M., Davis, J.M., Cheng, Y., Hu, Y.-S., and Ridge, K.M. (2023). Vimentin is required for tumor progression and metastasis in a mouse model of non–small cell lung cancer | Oncogene. Oncogene *42*, 2074–2087. https://doi.org/10.1038/s41388-023-02703-9.

39. Martinez-Quintanilla, J., Seah, I., Chua, M., and Shah, K. Oncolytic viruses: overcoming translational challenges. J Clin Invest *129*, 1407–1418. https://doi.org/10.1172/JCI122287.

40. Liang, Q., Luo, Z., Zeng, J., Chen, W., Foo, S.-S., Lee, S.-A., Ge, J., Wang, S., Goldman, S.A., Zlokovic, B.V., et al. (2016). Zika Virus NS4A and NS4B Proteins Deregulate Akt-mTOR Signaling in Human Fetal Neural Stem Cells to Inhibit Neurogenesis and Induce Autophagy. Cell Stem Cell *19*, 663–671. https://doi.org/10.1016/j.stem.2016.07.019.

41. Shah, P.S., Link, N., Jang, G.M., Sharp, P.P., Zhu, T., Swaney, D.L., Johnson, J.R., Von Dollen, J., Ramage, H.R., Satkamp, L., et al. (2018). Comparative flavivirus-host protein interaction mapping reveals mechanisms of dengue and Zika virus pathogenesis. Cell *175*, 1931-1945.e18. https://doi.org/10.1016/j.cell.2018.11.028.

42. Shiota, T., Li, T.-C., Nishimura, Y., Yoshizaki, S., Sugiyama, R., Shimojima, M., Saijo, M., Shimizu, H., Suzuki, R., Wakita, T., et al. (2019). Integrin α3 is involved in non-enveloped hepatitis E virus infection. Virology *536*, 119–124. https://doi.org/10.1016/j.virol.2019.07.025.

43. Akula, S.M., Pramod, N.P., Wang, F.-Z., and Chandran, B. (2002). Integrin α3β1 (CD 49c/29) Is a Cellular Receptor for Kaposi's Sarcoma-Associated Herpesvirus (KSHV/HHV-8) Entry into the Target Cells. Cell *108*, 407–419. https://doi.org/10.1016/S0092-8674(02)00628-1.

44. Li, Y., Li, F., Bai, X., Li, Y., Ni, C., Zhao, X., and Zhang, D. (2021). ITGA3 Is Associated With Immune Cell Infiltration and Serves as a Favorable Prognostic Biomarker for Breast Cancer. Front Oncol *11*, 658547. https://doi.org/10.3389/fonc.2021.658547.

45. Mutso, M., Saul, S., Rausalu, K., Susova, O., Žusinaite, E., Mahalingam, S., and Merits, A. (2017). Reverse genetic system, genetically stable reporter viruses and packaged subgenomic replicon based on a Brazilian Zika virus isolate. Journal of General Virology *98*, 2712–2724. https://doi.org/10.1099/jgv.0.000938.

46. Rodriguez, J., Haydinger, C.D., Peet, D.J., Nguyen, L.K., and von Kriegsheim, A. (2020). Asparagine Hydroxylation is a Reversible Post-translational Modification. Mol Cell Proteomics *19*, 1777–1789. https://doi.org/10.1074/mcp.ra120.002189.

47. Kammers, K., Cole, R.N., Tiengwe, C., and Ruczinski, I. (2015). Detecting Significant Changes in Protein Abundance. EuPA Open Proteom *7*, 11–19. https://doi.org/10.1016/j.euprot.2015.02.002.

48. Perez-Riverol, Y., Bandla, C., Kundu, D.J., Kamatchinathan, S., Bai, J., Hewapathirana, S., John, N.S., Prakash, A., Walzer, M., Wang, S., et al. (2025). The PRIDE database at 20 years: 2025 update. Nucleic Acids Res *53*, D543–D553. https://doi.org/10.1093/nar/gkae1011.

Figure Legends

Figure 1. Oncolytic effects of ZIKV infection in neuroblastoma tumorspheres

(A-B) Representative images at 8 dpi for SH-SY5Y (A) and IMR-32 (B) control tumorspheres or tumorspheres following infection with the ZIKV PRVABC59 or BeH819015 strain at an MOI of 2 or 10. (C-D) Quantification of tumorsphere area for SH-SY5Y (C) and IMR-32 (D) tumorspheres under the same conditions as in (A-B). Scale bar = 300 µm. $N = 3$ (biological replicates), $n \geq 2$ (technical replicates). Statistical significance indicators (asterisks) are shown for comparisons at 8 dpi. (E-F) 3D viability of individual SH-SY5Y (E) and IMR-32 (F) tumorspheres infected with the ZIKV PRVABC59 strain at an MOI of 2 or 10. $N = 3$ (biological replicates), $n \geq 3$ (technical replicates). (G-H) ZIKV titers in supernatants from individual SH-SY5Y (G) and IMR-32 (H) tumorspheres infected with the ZIKV PRVABC59 strain at an MOI of 2 or 10. $N = 3$ (biological replicates), $n \geq 3$ (technical replicates). Different symbol shapes represent different biological replicates. D0, D2, D4, and D6 represent 0, 2, 4, and 6 dpi, respectively. Data are presented as mean ± SD. Statistical significance was calculated using two-way ANOVA with Holm-Šidák multiple comparisons test. *$p < 0.05$; **$p < 0.01$; ****$p < 0.0001$. n.s. indicates no significance.

Figure 2. Transcriptome responses induced by ZIKV infection

(A-B) Volcano plots showing DEGs in SH-SY5Y (A) and IMR-32 (B) tumorspheres following infection with the ZIKV PRVABC59 strain at an MOI of 10. “padj” represents the adjusted *p*-value calculated using the Benjamini-Hochberg method. The dotted gray lines indicate the significance thresholds: $-\log_{10}\text{padj} = 2$ (equivalent to padj = 0.01). Red points represent significantly upregulated genes ($\log_2$ fold change > 0 and $-\log_{10}\text{padj} \geq 2$), while blue points represent significantly downregulated genes ($\log_2$fold change < 0 and $-\log_{10}\text{padj} \geq 2$). Gray points represent genes that are not significantly differentially expressed. The top 30 upregulated or downregulated genes, ranked by $-\log_{10}$padj, are labelled with their gene

symbols. (C) Heatmap showing significant KEGG pathways regulated by ZIKV infection in USP7, SH-SY5Y and IMR-32 models.

Figure 3. Effect of ZIKV non-structural proteins on tumorsphere formation

(A-C) Representative images (A), tumorsphere area (B), and 3D viability measurements (C) for SH-SY5Y tumorspheres formed by wild-type cells and cells transduced with GFP, NS1-GFP, NS2B-GFP, NS3-GFP, NS4A-GFP, NS4B-GFP, or NS5-GFP. (D-F) Representative images (D), tumorsphere area (E), and 3D viability measurements (F) for USP7 tumorspheres formed by the same cell lines. Tumorspheres were cultured for 12 days after seeding at 1 × 10^3 cells per well. Scale bar = 100 μm. N = 3 (biological replicates), n = 3 (technical replicates). Data are presented as mean ± SD. Statistical significance was calculated using one-way ANOVA with Dunnett's T3 multiple comparisons test, all compared to GFP. *p < 0.05; ***p < 0.001; ****p < 0.0001. n.s. indicates no significance.

Figure 4. Summary of the ZIKV-host PPI networks

(A) Overall workflow of affinity proteomics approach used to define ZIKV-host PPIs. (B-C) High-confidence ZIKV-host PPIs identified in SH-SY5Y (B) and USP7 cells (C). Viral baits (red or blue rectangles), host prey proteins (green circles), common prey shared between the two tumor types (pink borders), and virus-host interactions (gray lines) are shown. Proteins involved in different biological processes are colored as indicated. Protein complexes are highlighted with gray clusters on the map.

Figure 5. Comparative transcriptomics and affinity proteomics analysis

(A) Overlap of ZIKV-host PPI networks in SH-SY5Y and USP7 cells. (B) Overlap of GO cellular component terms between RNA-Seq and NS2B affinity proteomics datasets. (C) Interaction partners of NS2B enriched in focal adhesion GO cellular component term; gray lines represent physical interactions exported from STRING, and line thickness indicates the confidence level of each interaction.

Figure 6. Integrin α3 interacts with NS2B and NS4A

(A-B) Co-IP analysis confirming that integrin α3 and integrin β1 interact with NS2B and NS4A in SH-SY5Y (A) and USP7 cells (B). (C-F) Western blot images (C) and relative fold changes of integrin α3 (D), integrin β1 (E), and vimentin (F) expression regulated by GFP or ZIKV non-structural proteins in SH-SY5Y cells. N = 5 (biological replicates), n = 1 (technical replicates). (G-J) Western blot images (G) and relative fold changes of integrin α3 (H), integrin β1 (I), and vimentin (J) expression regulated by the same proteins as in (C-F) in USP7 cells. N = 3 (biological replicates), n = 1 (technical replicates). (K-L) Western blot images showing GFP expression in SH-SY5Y cells transduced with GFP, NS2B-GFP or NS4A-GFP under the following conditions: untreated, RISC-Free control (Ctrl siRNA), and *ITGA3* knockdown ($ITGA3^{KD}$) (K), with corresponding relative fold changes (L). N = 3 (biological replicates), n = 1 (technical replicates). (M-N) Western blot images (M) and corresponding relative fold changes (N) under the same conditions as in (K-L) for USP7 cells. N = 3 (biological replicates), n = 1 (technical replicates). All values are normalised to GAPDH control. Data are presented as mean ± SD. Statistical significance was calculated using one-way ANOVA with Dunnett's T3 multiple comparisons test. *$p < 0.05$; **$p < 0.01$. n.s. indicates no significance.

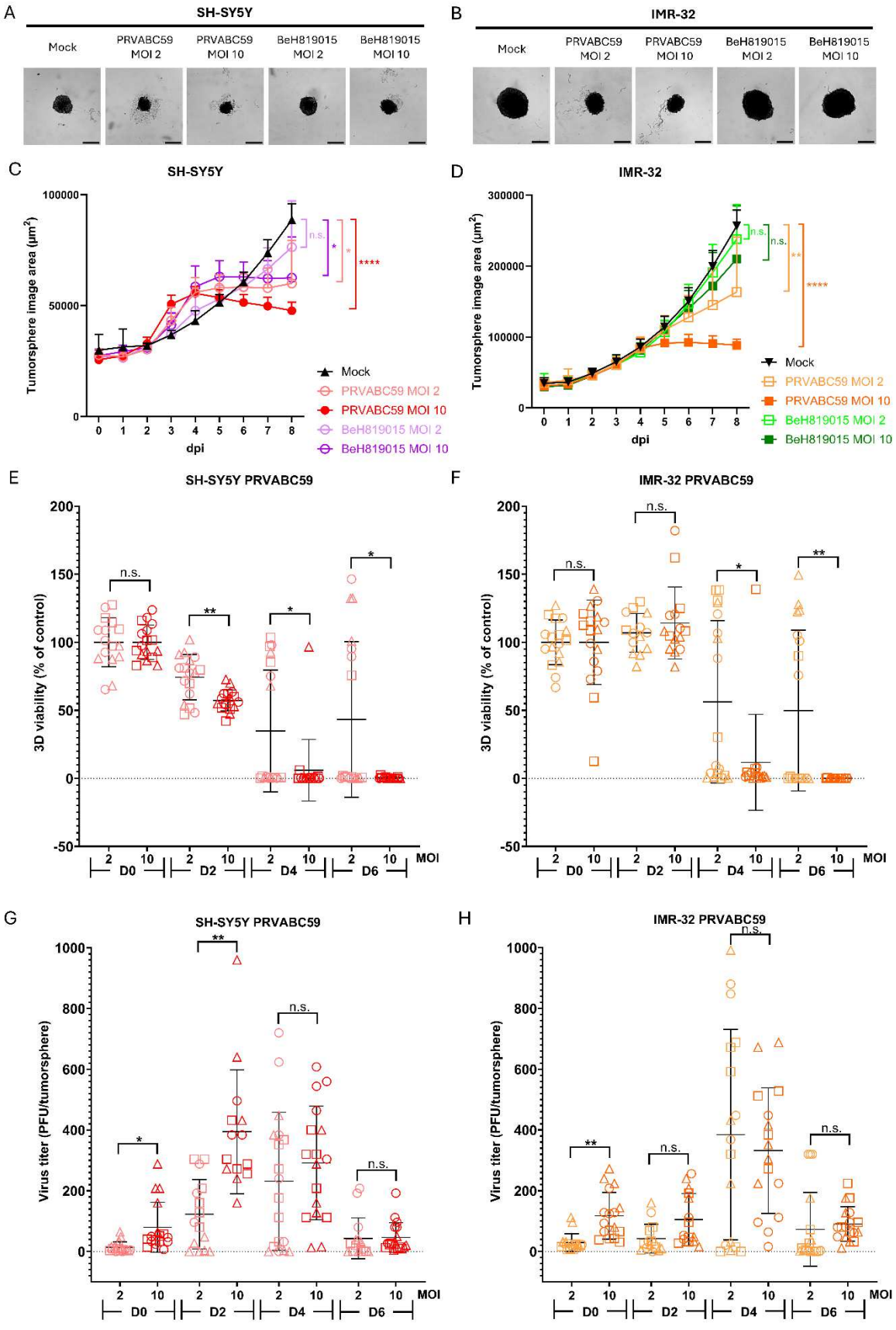
Figure 7. Effects of *ITGA3* knockdown on the regulation of tumorsphere formation by NS2B and NS4A

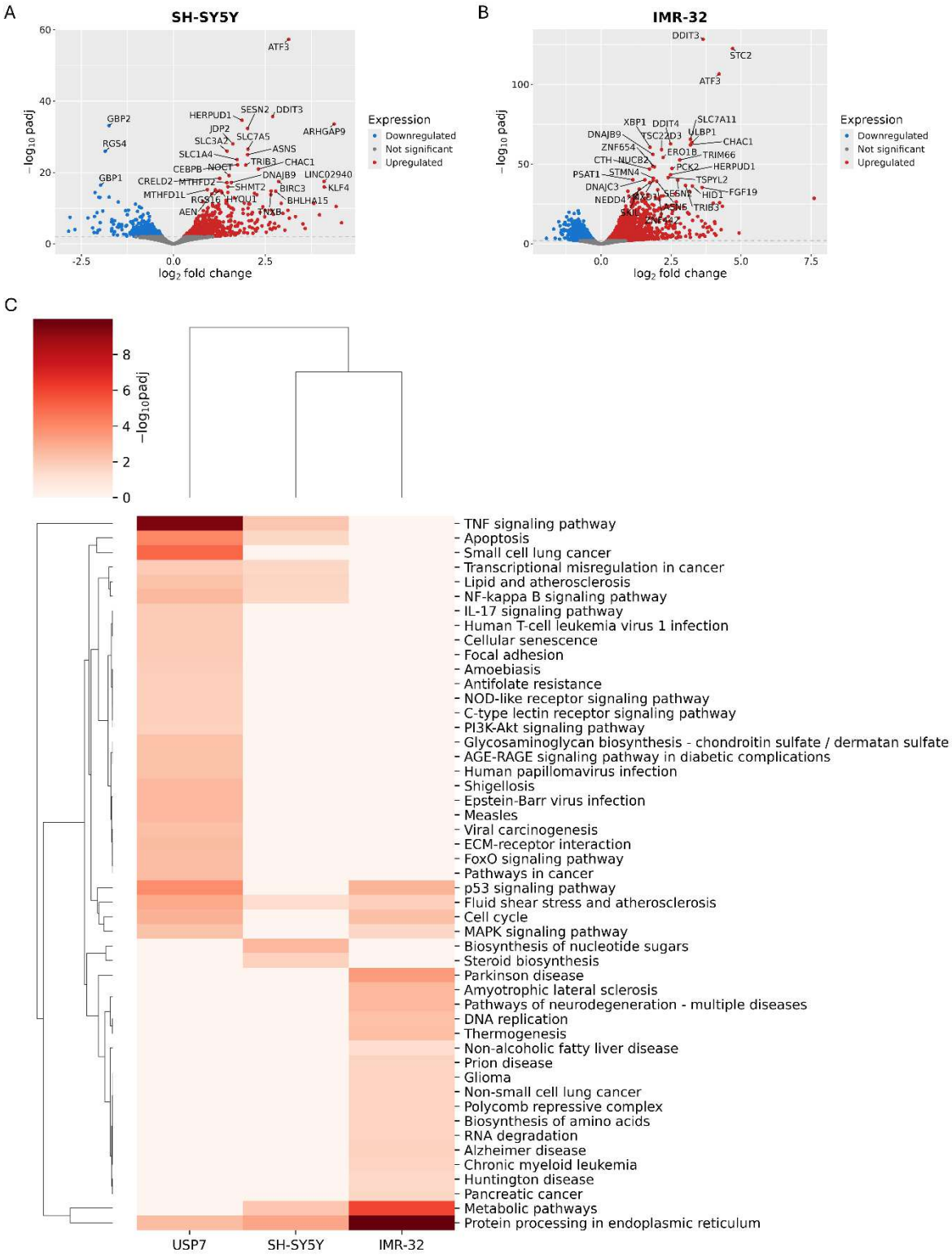
Tumorsphere formation assays were performed using wild-type cells and cells expressing GFP, NS2B, or NS4A under the following conditions: untreated, RISC-Free control (Ctrl siRNA), and *ITGA3* knockdown (ITGA3^{KD}). Tumorspheres were cultured for 12 days after seeding at 1 × 10³ cells per well. (A-B) Quantification of tumorsphere area for wild-type and GFP-expressing (A), or NS2B- and NS4A-expressing (B) SH-SY5Y tumorspheres. (C-D) Quantification of tumorsphere area for wild-type and GFP-expressing (C), or NS2B- and NS4A-expressing (D) USP7 tumorspheres. (E-F) Representative images of corresponding wild-type and GFP-expressing (E), or NS4A-expressing (F) USP7 tumorspheres. $N = 3$ (biological replicates), $n = 3$ (technical replicates). Scale bar = 100 μm. Data are presented as mean ± SD. Statistical significance was calculated using one-way ANOVA with Dunnett's T3 multiple comparisons test, all are compared to untreated wild-type cells. *$p < 0.05$; **$p < 0.01$; ***$p < 0.001$; ****$p < 0.0001$. n.s. indicates no significance.

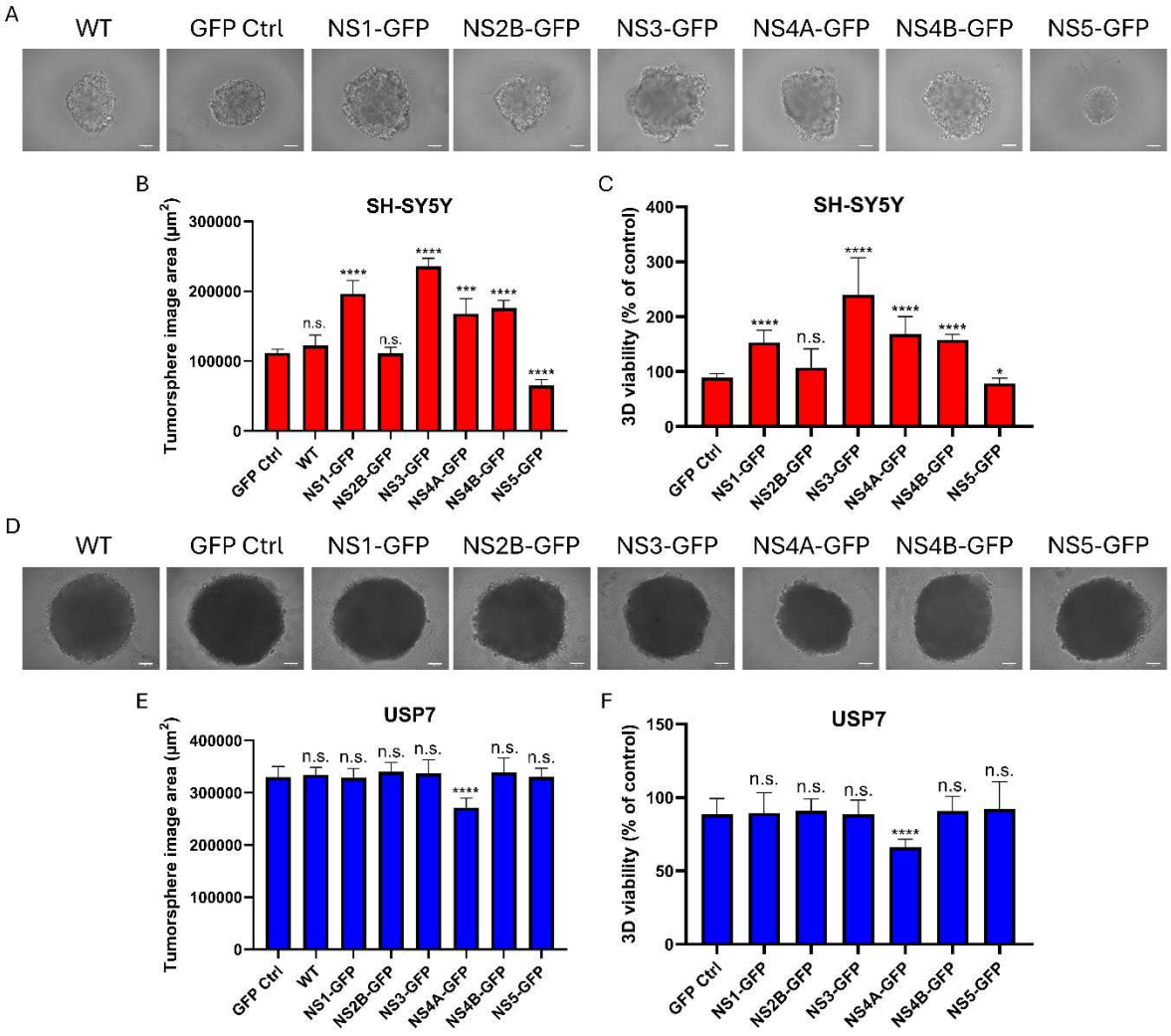
Figure 8. Effects of *ITGA3* knockdown on ZIKV oncolytic activity

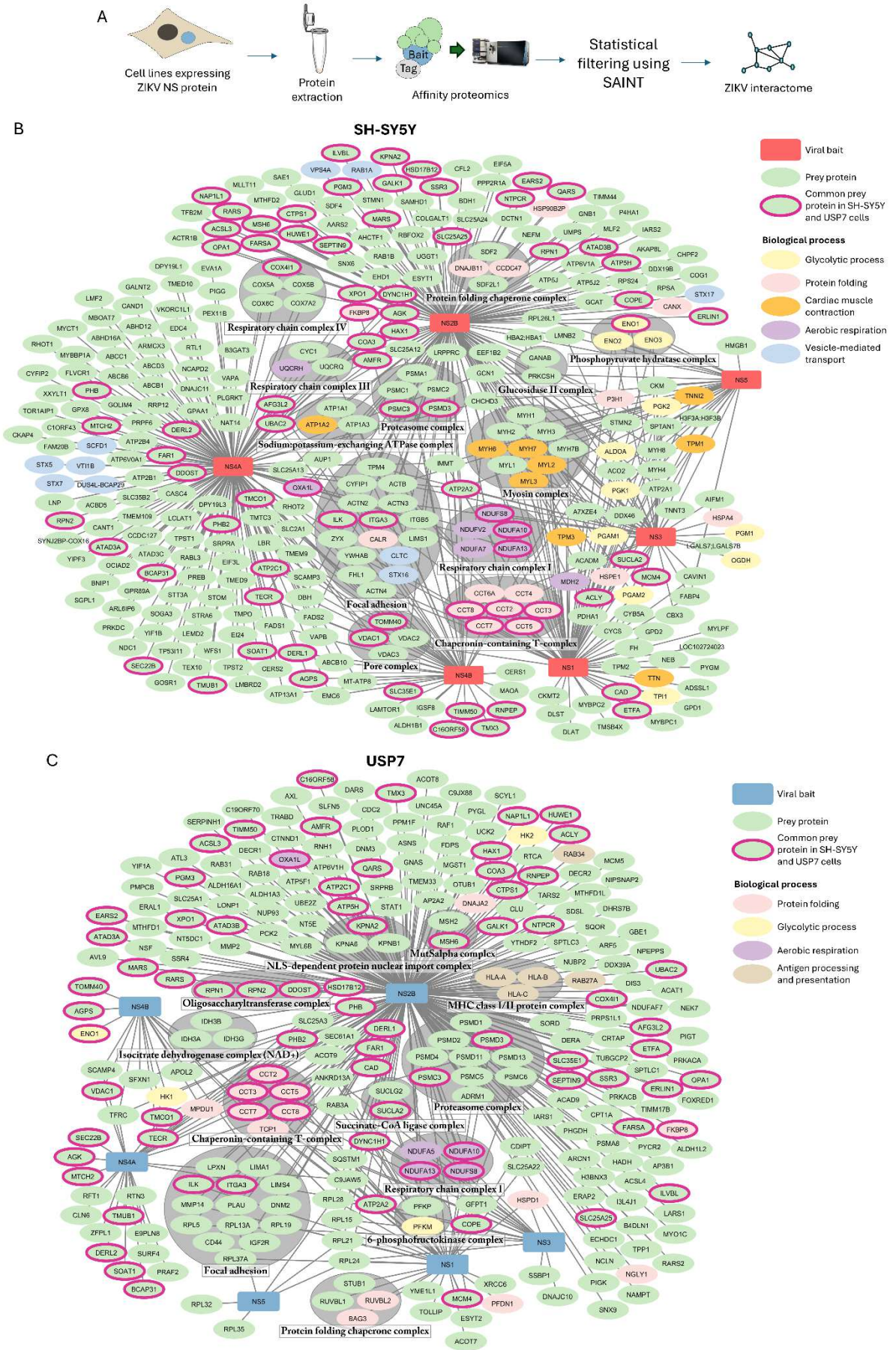
(A-B) Cell viability (A) and extracellular viral titres (B) in SH-SY5Y cell 2D cultures transfected with RISC-Free control (Ctrl siRNA) or *ITGA3* siRNA (ITGA3^{KD}) in the presence or absence of ZIKV infection. (C-E) Tumorsphere area normalized to d0 (C), 3D viability (D) and extracellular viral titres (E) in SH-SY5Y tumorspheres under the same treatments as in (A-B). (F-G) Cell viability (F) and extracellular viral titers (G) in USP7 cell 2D cultures under the same treatments as in (A-B). (H-J) Tumorsphere area normalized to d0 (H), 3D viability (I) and extracellular viral titres (J) in USP7 tumorspheres under the same treatments as in (A-B). (K-L) 3D invasion assay in USP7 tumorspheres treated as in (A), showing representative images (K) and the ratio of invading cell area to spheroid area (L) 4 days post-treatment. For (A-J): $N = 3$ (biological replicates), $n \geq 3$ (technical replicates); statistical significance was calculated using two-way ANOVA with Holm-Šidák multiple comparisons test. For (K-L): $N = 3$ (biological replicates), $n \geq 2$ (technical replicates); statistical significance was calculated using one-way ANOVA with Dunnett's T3 multiple comparisons

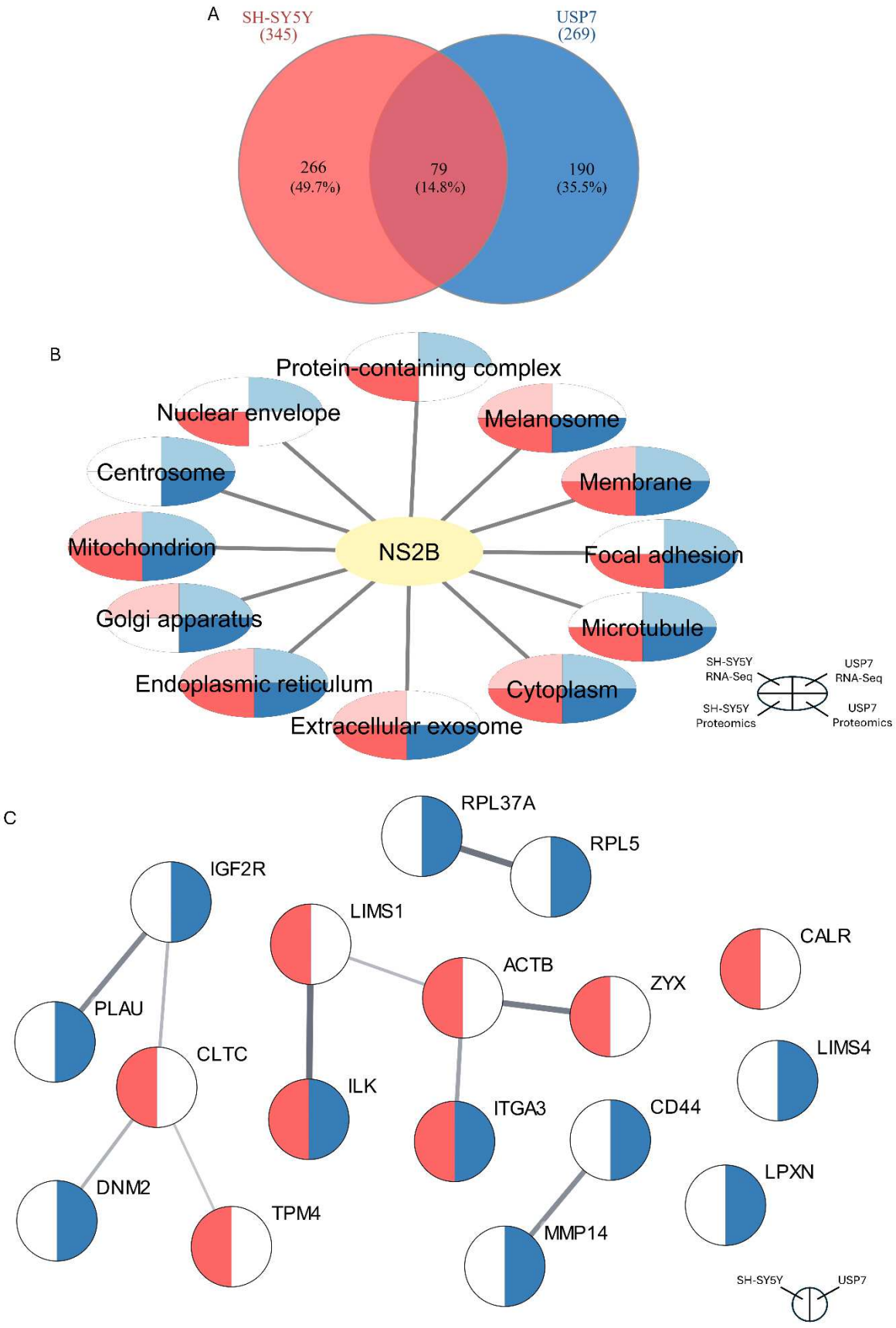
test. Data are presented as mean ± SD. Each table shows the statistical significance for the figure immediately to the left. For figures without a statistical significance table, asterisks in the figure indicate all significant comparisons between conditions, specifically highlighting differences between *ITGA3* knockdown in the presence of ZIKV infection and either ZIKV infection alone or ZIKV infection without knockdown. *$p < 0.05$; **$p < 0.01$; ***$p < 0.001$; ****$p < 0.0001$. n.s. indicates no significance.

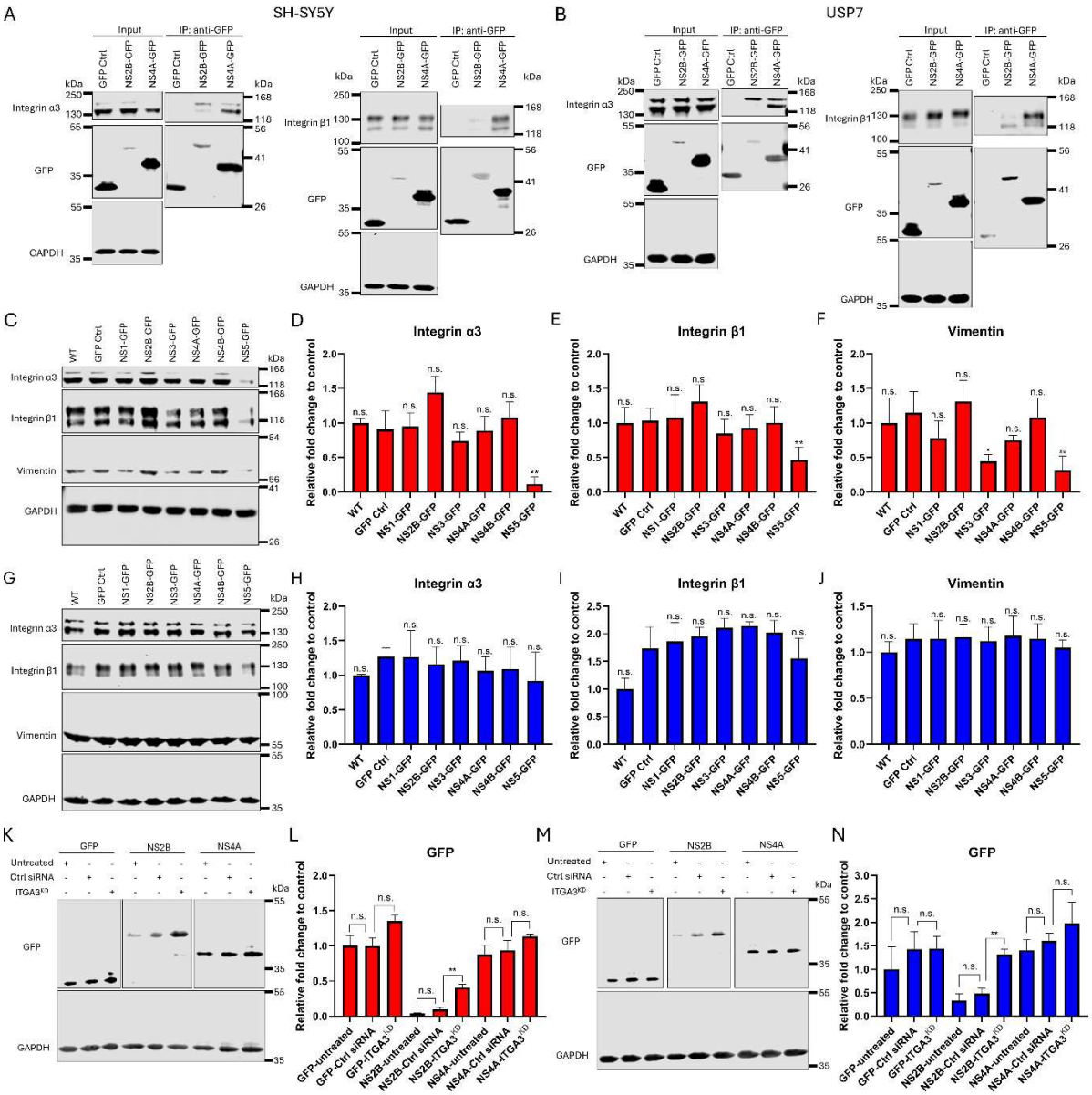

A
SH-SY5Y
Mock
PRVABC59 MOI 2
PRVABC59 MOI 10
BeH819015 MOI 2
BeH819015 MOI 10
B
IMR-32
C
SH-SY5Y
Tumorsphere image area (µm²)
dpi
Mock
PRVABC59 MOI 2
PRVABC59 MOI 10
BeH819015 MOI 2
BeH819015 MOI 10
D
IMR-32
E
SH-SY5Y PRVABC59
3D viability (% of control)
MOI
D0
D2
D4
D6
F
IMR-32 PRVABC59
G
SH-SY5Y PRVABC59
Virus titer (PFU/tumorsphere)
H
IMR-32 PRVABC59

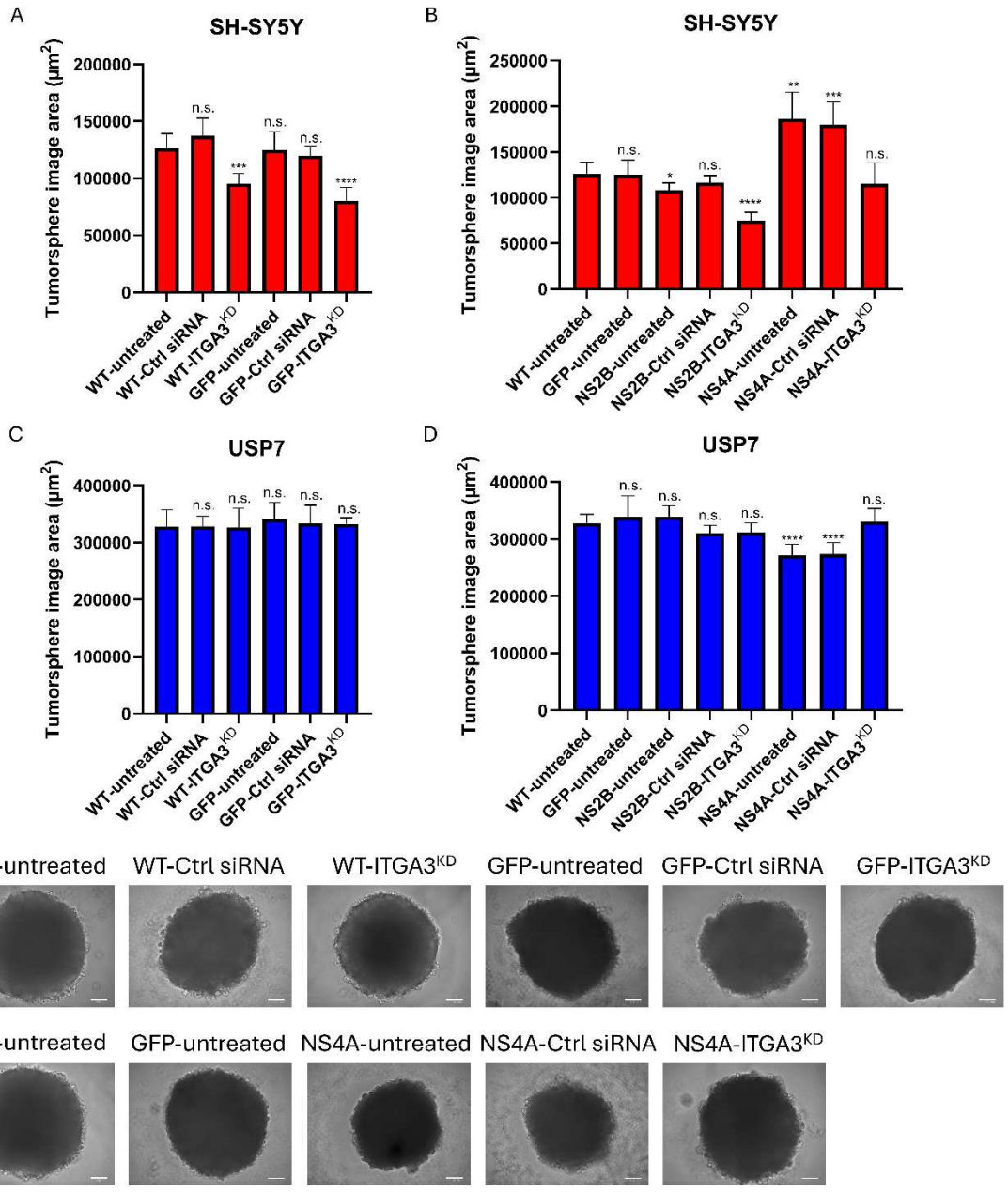

A
SH-SY5Y
ATF3
GBP2
HERPUD1
SESN2
DDIT3
JDP2
SLC7A5
ARHGAP9
RGS4
SLC3A2
ASNS
SLC1A4
TRIB3
CHAC1
CEBPB
NOCT
GBP1
CRELD2
MTHFD2
DNAJB9
LINC02940
SHMT2
BIRC3
KLF4
MTHFD1L
RGS16
HYOU1
BHLHA15
AEN
TNXB
Expression
Downregulated
Not significant
Upregulated
−log10 padj
log2 fold change
B
IMR-32
DDIT3
STC2
ATF3
XBP1
DDIT4
SLC7A11
DNAJB9
TSC22D3
ULBP1
CHAC1
ZNF654
ERO1B
TRIM66
CTH
NUCB2
PCK2
HERPUD1
PSAT1
STMN4
TSPYL2
DNAJC3
NEDD4
HID1
FGF19
TRIB3
C
−log10padj
TNF signaling pathway
Apoptosis
Small cell lung cancer
Transcriptional misregulation in cancer
Lipid and atherosclerosis
NF-kappa B signaling pathway
IL-17 signaling pathway
Human T-cell leukemia virus 1 infection
Cellular senescence
Focal adhesion
Amoebiasis
Antifolate resistance
NOD-like receptor signaling pathway
C-type lectin receptor signaling pathway
PI3K-Akt signaling pathway
Glycosaminoglycan biosynthesis - chondroitin sulfate / dermatan sulfate
AGE-RAGE signaling pathway in diabetic complications
Human papillomavirus infection
Shigellosis
Epstein-Barr virus infection
Measles
Viral carcinogenesis
ECM-receptor interaction
FoxO signaling pathway
Pathways in cancer
p53 signaling pathway
Fluid shear stress and atherosclerosis
Cell cycle
MAPK signaling pathway
Biosynthesis of nucleotide sugars
Steroid biosynthesis
Parkinson disease
Amyotrophic lateral sclerosis
Pathways of neurodegeneration - multiple diseases
DNA replication
Thermogenesis
Non-alcoholic fatty liver disease
Prion disease
Glioma
Non-small cell lung cancer
Polycomb repressive complex
Biosynthesis of amino acids
RNA degradation
Alzheimer disease
Chronic myeloid leukemia
Huntington disease
Pancreatic cancer
Metabolic pathways
Protein processing in endoplasmic reticulum
USP7
SH-SY5Y
IMR-32


A
WT
GFP Ctrl
NS1-GFP
NS2B-GFP
NS3-GFP
NS4A-GFP
NS4B-GFP
NS5-GFP
B
SH-SY5Y
Tumorsphere image area (μm²)
300000
200000
100000
0
n.s.
****
***
C
SH-SY5Y
3D viability (% of control)
400
300
200
100
0
*
D
E
USP7
400000
n.s.
F
USP7
150
50

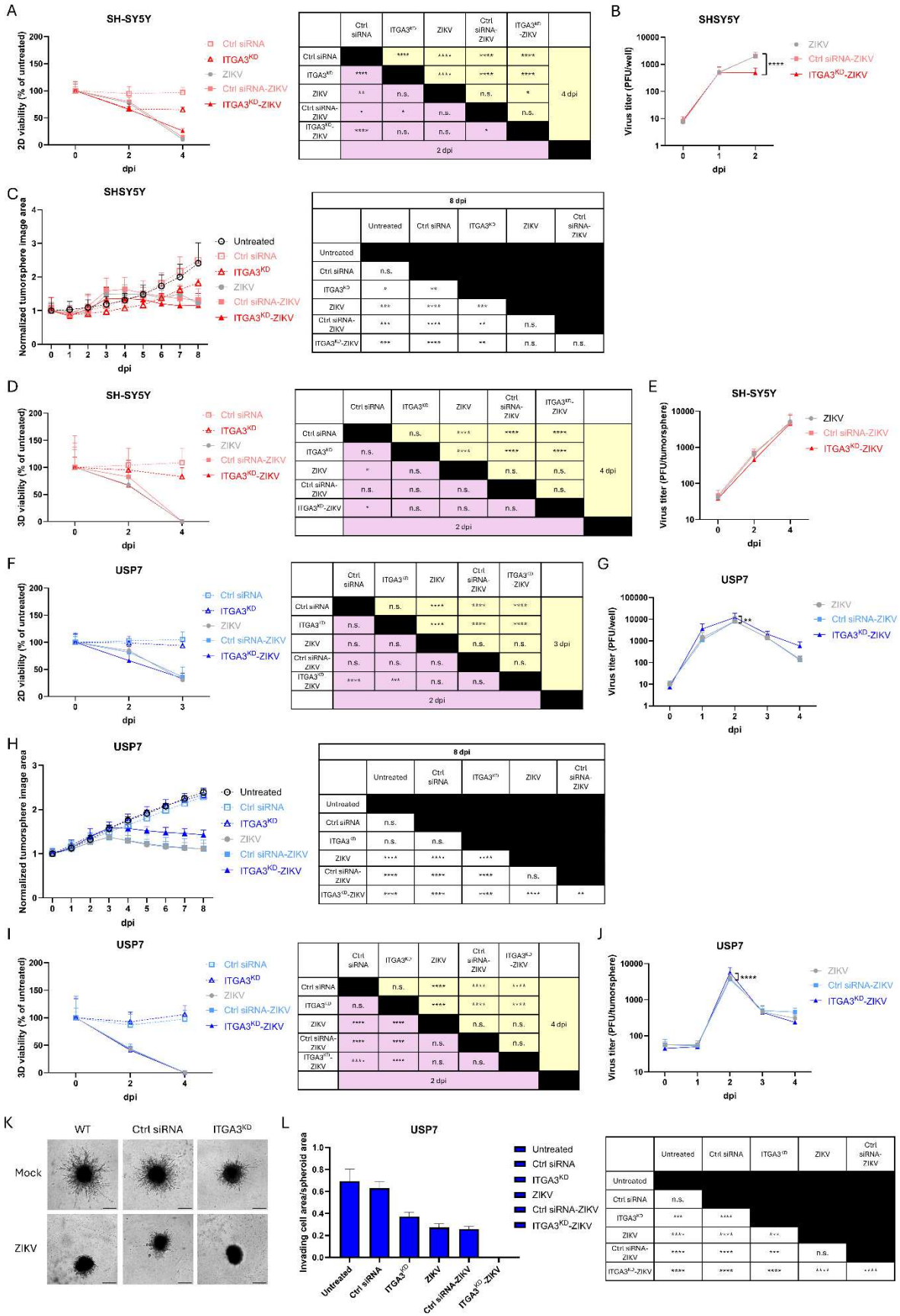

A
Cell lines expressing ZIKV NS protein
Protein extraction
Bait
Tag
Affinity proteomics
Statistical filtering using SAINT
ZIKV interactome
B
SH-SY5Y
Viral bait
Prey protein
Common prey protein in SH-SY5Y and USP7 cells
Biological process
Glycolytic process
Protein folding
Cardiac muscle contraction
Aerobic respiration
Vesicle-mediated transport
Protein folding chaperone complex
Respiratory chain complex IV
Phosphopyruvate hydratase complex
Respiratory chain complex III
Glucosidase II complex
Proteasome complex
Sodium:potassium-exchanging ATPase complex
Myosin complex
Respiratory chain complex I
Focal adhesion
Chaperonin-containing T-complex
Pore complex
C
USP7
Viral bait
Prey protein
Common prey protein in SH-SY5Y and USP7 cells
Biological process
Protein folding
Glycolytic process
Aerobic respiration
Antigen processing and presentation
NLS-dependent protein nuclear import complex
MutSalpha complex
Oligosaccharyltransferase complex
MHC class I/II protein complex
Isocitrate dehydrogenase complex (NAD+)
Proteasome complex
Succinate-CoA ligase complex
Chaperonin-containing T-complex
Respiratory chain complex I
6-phosphofructokinase complex
Focal adhesion
Protein folding chaperone complex


A
SH-SY5Y
(345)
USP7
(269)
266
(49.7%)
79
(14.8%)
190
(35.5%)
B
Protein-containing complex
Nuclear envelope
Melanosome
Centrosome
Membrane
Mitochondrion
NS2B
Focal adhesion
Golgi apparatus
Microtubule
Endoplasmic reticulum
Cytoplasm
Extracellular exosome
SH-SY5Y
RNA-Seq
USP7
RNA-Seq
SH-SY5Y
Proteomics
USP7
Proteomics
C
RPL37A
RPL5
IGF2R
LIMS1
CALR
ACTB
ZYX
PLAU
CLTC
LIMS4
ILK
ITGA3
CD44
DNM2
TPM4
LPXN
MMP14
SH-SY5Y
USP7


A
SH-SY5Y
Input
IP: anti-GFP
GFP Ctrl
NS2B-GFP
NS4A-GFP
kDa
Integrin α3
Integrin β1
GFP
GAPDH
B
USP7
C
WT
NS1-GFP
NS3-GFP
NS4B-GFP
NS5-GFP
Vimentin
D
Integrin α3
E
Integrin β1
F
Vimentin
Relative fold change to control
n.s.
G
H
I
J
K
Untreated
Ctrl siRNA
ITGA3KD
L
GFP
M
N
GFP-untreated
GFP-Ctrl siRNA
GFP-ITGA3KD
NS2B-untreated
NS2B-Ctrl siRNA
NS2B-ITGA3KD
NS4A-untreated
NS4A-Ctrl siRNA
NS4A-ITGA3KD


A
SH-SY5Y
Tumorsphere image area (μm²)
200000
150000
100000
50000
0
n.s.
n.s.
***
n.s.
n.s.
****
WT-untreated
WT-Ctrl siRNA
WT-ITGA3KD
GFP-untreated
GFP-Ctrl siRNA
GFP-ITGA3KD
B
SH-SY5Y
Tumorsphere image area (μm²)
250000
200000
150000
100000
50000
0
n.s.
n.s.
*
n.s.
****
**
***
n.s.
WT-untreated
GFP-untreated
NS2B-untreated
NS2B-Ctrl siRNA
NS2B-ITGA3KD
NS4A-untreated
NS4A-Ctrl siRNA
NS4A-ITGA3KD
C
USP7
Tumorsphere image area (μm²)
400000
300000
200000
100000
0
n.s.
n.s.
n.s.
n.s.
n.s.
WT-untreated
WT-Ctrl siRNA
WT-ITGA3KD
GFP-untreated
GFP-Ctrl siRNA
GFP-ITGA3KD
D
USP7
Tumorsphere image area (μm²)
400000
300000
200000
100000
0
n.s.
n.s.
n.s.
n.s.
****
****
n.s.
WT-untreated
GFP-untreated
NS2B-untreated
NS2B-Ctrl siRNA
NS2B-ITGA3KD
NS4A-untreated
NS4A-Ctrl siRNA
NS4A-ITGA3KD

E
WT-untreated
WT-Ctrl siRNA
WT-ITGA3KD
GFP-untreated
GFP-Ctrl siRNA
GFP-ITGA3KD
F
WT-untreated
GFP-untreated
NS4A-untreated
NS4A-Ctrl siRNA
NS4A-ITGA3KD


A
SH-SY5Y
2D viability (% of untreated)
dpi
Ctrl siRNA
ITGA3KD
ZIKV
Ctrl siRNA-ZIKV
ITGA3KD-ZIKV
4 dpi
2 dpi
B
SHSY5Y
Virus titer (PFU/well)
C
SHSY5Y
Normalized tumorsphere image area
Untreated
8 dpi
D
SH-SY5Y
3D viability (% of untreated)
E
SH-SY5Y
Virus titer (PFU/tumorsphere)
F
USP7
3 dpi
G
USP7
H
USP7
I
USP7
J
USP7
K
WT
Ctrl siRNA
ITGA3KD
Mock
ZIKV
L
USP7
Invading cell area/spheroid area

Supplemental information

Table S1. List of DEGs in SH-SY5Y tumorspheres

Table S2. List of DEGs in IMR-32 tumorspheres

Table S3. List of interactomes in SH-SY5Y cells

Table S4. List of interactomes in USP7 cells

Document S1. Table S5 and Figures S1–S6

Supplementary Files

This is a list of supplementary files associated with this preprint. Click to download.

- TableS1.ListofDEGsinSHSY5Ytumorspheres.xlsx
- TableS3.ListofinteractomesinSHSY5Ycells.xlsx
- DocumentS1.pdf
- TableS2.ListofDEGsinIMR32tumorspheres.xlsx
- TableS4.ListofinteractomesinUSP7cells.xlsx